

## Electronic consequences of random layer-thickness fluctuations in AIAs/GaAs superlattices

Kurt A. Mäder, Lin-Wang Wang, and Alex Zunger

Citation: *Journal of Applied Physics* **78**, 6639 (1995); doi: 10.1063/1.360728

View online: <http://dx.doi.org/10.1063/1.360728>

View Table of Contents: <http://scitation.aip.org/content/aip/journal/jap/78/11?ver=pdfcov>

Published by the [AIP Publishing](#)

---

### Articles you may be interested in

[Effect of disorder-induced band mixing on the conduction-band effective mass of InAlGaAs alloys lattice matched to InP](#)

*J. Appl. Phys.* **80**, 1239 (1996); 10.1063/1.362862

[Planar disorder- and native-oxide-defined photopumped AIAs–GaAs superlattice minidisk lasers](#)

*J. Appl. Phys.* **79**, 8204 (1996); 10.1063/1.362460

[Ordered and randomly disordered AIAs/GaAs short-period superlattices](#)

*J. Vac. Sci. Technol. B* **12**, 1009 (1994); 10.1116/1.587116

[Random telegraph fluctuations in GaAs/Al<sub>0.4</sub>Ga<sub>0.6</sub>As resonant tunneling diodes](#)

*AIP Conf. Proc.* **285**, 194 (1993); 10.1063/1.44573

[Interband optical absorption in amorphous semiconductors](#)

*AIP Conf. Proc.* **120**, 371 (1984); 10.1063/1.34766

---

Frustrated by old technology?

Is your AFM dead and can't be repaired?

Sick of bad customer support?

**It is time to upgrade your AFM**

Minimum \$20,000 trade-in discount for purchases before August 31st

Asylum Research is today's technology leader in AFM

**OXFORD INSTRUMENTS**  
The Business of Science®

[dropmyoldAFM@oxinst.com](mailto:dropmyoldAFM@oxinst.com)

# Electronic consequences of random layer-thickness fluctuations in AlAs/GaAs superlattices

Kurt A. Mäder,<sup>a)</sup> Lin-Wang Wang, and Alex Zunger  
National Renewable Energy Laboratory, Golden, Colorado 80401

(Received 12 June 1995; accepted for publication 24 August 1995)

We study the effects of a few types of atomic disorder on the electronic and optical properties of AlAs/GaAs (001) and (111) superlattices: (i) atomic intermixing across the interfaces; (ii) replacing a single monolayer in a superlattice by one containing the opposite atomic type (isoelectronic  $\delta$  doping); and (iii) random layer-thickness fluctuations in superlattices (SL). Type (i) is an example of lateral disorder, while types (ii) and (iii) are examples of vertical disorder. Using three-dimensional empirical pseudopotential theory and a plane-wave basis, we calculate the band gaps, electronic wave functions, and optical matrix elements for systems containing up to 2000 atoms in the computational unit cell. Spin-orbit interactions are omitted. Computationally much less costly effective-mass calculations are used to evaluate the density of states and eigenstates away from the band edges in vertically disordered SLs. Our main findings are: (i) Chemical intermixing across the interface can significantly shift the SL energy levels and even change the identity (e.g., symmetry) of the conduction-band minimum in AlAs/GaAs SLs; (ii) any amount of thickness fluctuations in SLs leads to band-edge wave-function localization; (iii) these fluctuation-induced bound states will emit photons at energies below the “intrinsic” absorption edge (red shift of photoluminescence); (iv) monolayer fluctuations in thick superlattices create a gap level whose energy is pinned at the value produced by a single  $\delta$  layer with “wrong” thickness; (v) (001) AlAs/GaAs SLs with monolayer thickness fluctuations have a direct band gap, while the ideal (001) superlattices are indirect for  $n < 4$ ; (vi) there is no mobility edge for vertical transport in a disordered superlattice, because all the states are localized; however, the density of states retains some of the features of the ordered-superlattice counterpart. We find quantitative agreement with experiments on intentionally disordered SLs [A. Sasaki, *J. Cryst. Growth* **115**, 490 (1991)], explaining the strong intensity and large red shift of the photoluminescence in the latter system. We provide predictions for the case of unintentional disorder. © 1995 American Institute of Physics.

## I. INTRODUCTION

Experimental and theoretical research on semiconductor superlattices (SL) has, for a long time, focused on ideal, periodic structures: Growers attempt to achieve SLs with atomically abrupt interfaces having fixed, predetermined layer thicknesses  $n$  and  $m$  of the two materials  $A$  and  $G$ , respectively, while theorists calculated the electronic structure of these ideal structures by applying periodic boundary conditions to a small SL unit cell  $(A)_n/(G)_m$ . Possible conflicts between experiment (e.g., spectroscopy) and theory (e.g., envelope function  $k \cdot p$ ) are often settled by adjusting some of the theoretical fitting parameters (band offsets, Luttinger parameters, layer thicknesses), thus restoring agreement with experiment. In recent years, attention has shifted somewhat away from ideal to nonideal SLs in two ways: First, with the advent of more sensitive characterization techniques, it has become evident that not only are semiconductor interfaces almost never ideal, but that this unintentional disorder in real samples has discernible spectroscopic and transport consequences<sup>1-10</sup> that should be taken into account by theory. Second, *intentionally* disordered SLs have been

proposed<sup>11,12</sup> and grown,<sup>13-15</sup> revealing very interesting disorder-induced effects on the electronic, transport, and optical properties.

Disorder in a SL can be broadly classified in two categories:

- (i) Lateral disorder in the  $(x,y)$  substrate plane<sup>1-5</sup> [Fig. 1(a)], and
- (ii) Vertical disorder along the SL growth direction ( $z$ ) in the form of discrete layer-thickness fluctuations<sup>6-10</sup> [Fig. 1(b)].

Lateral disorder occurs in the form of chemically intermixed interfaces,<sup>1-3</sup> steps,<sup>4</sup> or islands<sup>5</sup> protruding from material  $A$  into  $G$ , and vice versa. The translational symmetry of the SL is broken in the  $(x,y)$  plane. When averaging over the composition fluctuations in the  $(x,y)$  plane, lateral disorder produces a graded, continuous composition profile along the  $z$  axis. Thus, if all of the interfaces in a laterally disordered SL are equivalent, the one-dimensional (1D) periodicity along the growth direction is preserved on average.

Vertical disorder, on the other hand, is characterized by a discrete composition profile along  $z$ . Here the interfaces are reasonably flat in the  $(x,y)$  plane, but the  $A$  and  $G$  layer thicknesses fluctuate around their nominal values. The translational symmetry of the SL along  $z$  is broken, and the dis-

<sup>a)</sup>Present address: Centre Européen de Calcul Atomique et Moléculaire, Ecole Normale Supérieure, 46, Allée d'Italie, 69364 Lyon Cedex 07, France; Electronic mail: mader@cecam.fr

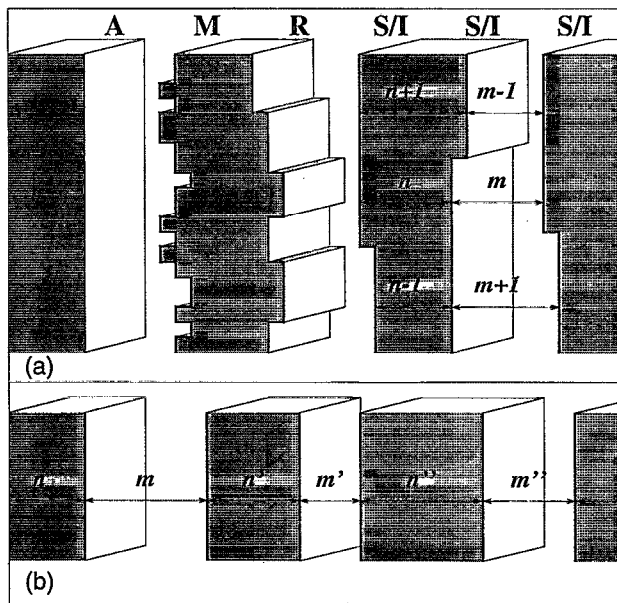


FIG. 1. Schematic representation of various types of disorder in nonideal  $(A)_n/(G)_m$  superlattices: (a) lateral disorder in the interface plane; (b) vertical disorder along the superlattice orientation. The interface structures sketched in cross section in (a) are atomically abrupt (A), “microrough” or intermixed (M), rough (R), and stepped or islanded (S/I). (The latter cannot be distinguished in cross section.) In (b) the layer thicknesses fluctuate, assuming integer values  $n, m, n', m', n'', m'', \dots$  monolayers, while the individual interfaces are atomically flat. “Extended” regions in (a) of uniform layer thicknesses  $n, m, n \pm 1, m \pm 1, \dots$  between stepped/islanded interfaces are indicated with arrows.

order is “quasi one dimensional” (which does not mean, however, that the Schrödinger equation can be separated into a 1D disordered and a 2D ordered system).

Unintentional disorder is likely to consist of both types of disorder.<sup>16,17</sup> The experimentally observable types of disorder depend critically on the coherence length of the experimental probe (x-ray diffraction, electron microscopy, Raman scattering, etc.). Lateral disorder, for example, has been shown to exhibit a rather complex “roughness spectrum,” i.e., interface roughness occurs on many different length scales.<sup>4,18</sup> If the roughness spectrum is bimodal<sup>18</sup> having both a small (“microroughness”) and large (steps, islands) size scales, and the coherence length of the probe is much larger than the small roughness scale, but smaller than the large roughness scale, then the probe will “see” an ensemble of different layer thicknesses.<sup>16</sup> Photoluminescence spectra of multiple quantum wells have often been rationalized in these terms, because they exhibited a set of rather sharp emission lines that could be attributed to excitonic transitions in quantum wells of various thicknesses.<sup>7,10,19</sup> If the probe involves excitation of a valence hole or a conduction electron in a cubic semiconductor, its response will predominantly reflect the small length scales (of the order of a few lattice constants). Therefore, if lateral imperfections occur in the form of atomic intermixing, the effect on the SL band structure is noticeable predominantly in short-period SLs, but less significant in long-period SLs or multiple quantum wells (where the electrons “see” mostly bulk, and little interface).

If, on the other hand, lateral imperfections consist of large islands, or well-separated steps, the system resembles, in terms of the electronic structure, a SL with vertical thickness fluctuations, since the electrons experience layers of definite, but fluctuating, thickness that extend in the  $(x, y)$  plane [see the interfaces labeled “S/I” in Fig. 1(a)].

Intentional disorder has been studied mostly in the form of vertical disorder.<sup>13–15</sup> The general procedure is to define certain constraints (“rules”) on the layer thicknesses, and to use a random-number generator to establish a particular growth sequence obeying these constraints (see Sec. II). Lateral disorder (e.g., interdiffusion) is unwanted in this case, and great care is taken to assess the effects of any possible lateral imperfections that could interfere with the wanted effects of random vertical disorder.

Theoretical studies on nonideal semiconductor SLs have largely concentrated on strictly one-dimensional one-band models, such as Kronig–Penney models using the effective-mass approximation (EMA),<sup>20–24</sup> or one-dimensional tight-binding models.<sup>11,25,26</sup> Within 1D models, lateral imperfections are simulated by graded, continuous potential profiles corresponding to composition profiles averaged in the  $(x, y)$  plane.<sup>27,28</sup> Vertical disorder, on the other hand, can be studied in the form of mathematically 1D models, if one is willing to ignore the truly 3D crystal structure of a SL. A vast literature exists on localization in 1D disordered systems,<sup>29,30</sup> and many exact analytic results have emerged.<sup>31–33</sup> For example, it is well established that in a one-dimensional disordered system all states are in general localized.<sup>34</sup> Exceptions to this rule exist for *deterministic* forms of 1D disorder,<sup>32</sup> some of which have been realized experimentally in 3D SLs, e.g., AlAs/GaAs Fibonacci SLs.<sup>13,35,36</sup>

Studies on nonideal SLs using three-dimensional band-structure theories are scarce, because large computational unit cells are required to simulate the absence of periodicity in one, two, or even three dimensions. For example, atomic intermixing in  $(\text{AlAs})_1/(\text{GaAs})_1$  (001) SLs has been studied using the local-density approximation (LDA) by considering reconstructed interfacial unit cells with atomic swaps across the interface.<sup>37</sup> 3D tight-binding calculations on disordered SLs were described by Wang *et al.*,<sup>38–40</sup> and on quasiperiodic SLs by Hirose and co-workers<sup>36</sup> and by Kumar and Ananthakrishna.<sup>41</sup> Chen and Xiong<sup>42</sup> used a four-band Luttinger–Kohn Hamiltonian to calculate the hole subband structure in disordered AlAs/GaAs SLs.

In this article we present 3D electronic structure calculations on AlAs/GaAs (001) and (111) SLs with fluctuating layer thicknesses (vertical disorder) and with interfacial roughness (lateral disorder), thus simulating both intentional and unintentional thickness fluctuations. A 3D description of the energy bands is particularly important for short-period AlAs/GaAs SLs, because of strong coupling between bands originating from different points in the Brillouin zone. Disordered SLs have shown surprising and unique optical properties relative to their ordered counterparts with the same composition:

- (a) strong and initially fast decaying (lifetime  $\tau = 0.25$  ns at  $T = 77$  K) photoluminescence (PL) intensity<sup>43</sup> even

though the equivalent ordered  $(\text{AlAs})_2/(\text{GaAs})_2$  SL has an indirect band gap and thus emits both weakly and slowly;

- (b) A large red shift ( $\sim 60$  meV) of the PL peak<sup>44,45</sup> with respect to the equivalent  $o$ -SL;
- (c) An order-of-magnitude slower rate of reduction of the PL intensity with temperature,<sup>46</sup> and
- (d) Nonexponential PL intensity decay at long times<sup>45</sup> ( $\sim \mu\text{s}$ ).

These unusual properties of  $d$ -SLs appear very attractive for optoelectronic applications.<sup>44</sup> A short account of our results on these two types of intentionally disordered SLs has been published in Ref. 47.

In modeling the electronic structure of a  $d$ -SL, one faces difficulties arising from the existence of two entirely different length scales:

- (i) The lack of translational symmetry requires the use of unit cells with a macroscopic length  $N \approx 1000$  monolayers (ML), equal to the total length of the  $d$ -SL ( $Nd \approx 300$  nm, where  $d$  is the monolayer thickness);
- (ii) The spatial variations of the electron potential, however, occur on a microscopic length scale of about 0.1 nm.

While it is possible to rescale the microscopic length scale by replacing the periodic atomic potential by an external, rectangular potential, this approach fails to describe important features of the band structure [e.g., the indirect gap of the  $(\text{AlAs})_2/(\text{GaAs})_2$   $o$ -SL] in the present regime of rapid layer fluctuations. To overcome the problems arising from the existence of two disparate length scales, we extended a microscopic pseudopotential description of the electron structure to a macroscopic length scale necessitated by the absence of translational symmetry. We use fixed (screened) atomic pseudopotentials that were carefully fitted to bulk band structures, effective masses, deformation potentials, band offsets, and energy levels in superlattices.<sup>48</sup> This is also called the empirical pseudopotential method (EPM) in the following. The wave functions are expanded in a basis of plane waves. We solve the Schrödinger problem using the “folded-spectrum” method,<sup>49</sup> where eigenstates are obtained directly in an energy window of interest (e.g., near the band gap), without having to solve for any of the lower-lying eigenstates first, thus circumventing the need for orthogonalization. The effort scales linearly with the number of atoms, allowing us to use the realistic, three-dimensional pseudopotentials, and to solve the Schrödinger equation in a highly flexible plane-wave basis even for  $N = 1000$  ML. Following these accurate pseudopotential calculations, we also performed EMA calculations

- (i) to check the validity of the effective mass method, and
- (ii) to obtain some statistical properties of the electronic states away from the band edge.

The remainder of the article is organized as follows. In Sec. II we describe the structure of the studied SLs. The electronic Hamiltonians are discussed in Sec. III. In Sec. IV

pseudopotential and 1D effective-mass results on disordered SLs are presented. Conclusions and a summary are presented in Sec. V.

## II. MODELING THE STRUCTURE OF SUPERLATTICES WITH RANDOM LAYER-THICKNESS FLUCTUATIONS

An ordered, ideal superlattice is characterized by a unit cell  $A_n/G_m$  that is repeated periodically, and which contains  $n$  monolayers of material  $A$  and  $m$  monolayers of material  $G$ , respectively. The repeat period of the SL is  $M = n + m$ . If, however, instead of the periodic sequence  $n, m, n, m, \dots$  we have random layer-thickness fluctuations, the growth sequence is given by  $n, m, n', m', n'', m'', \dots$ , where the individual layer thicknesses are no longer repeated periodically [see Fig. 1(b)]. The SL is thus no longer described by the small,  $n + m$  atoms unit cell  $A_n/G_m$ . Instead, we use a large unit cell that can be described by (normalized) distribution functions  $p_A(n)$  and  $p_G(m)$  denoting the probability of finding a layer of material  $\alpha = A$ , or  $\alpha = G$  with thickness of  $n$  monolayers. We usually require that an  $A$  layer will be followed by a  $G$  layer, and vice versa. [This constraint can, however, be easily relaxed by allowing  $p_\alpha(0) > 0$ . For example,  $p_G(0) > 0$  means “skip a layer of material  $G$ ” with probability  $p_G(0)$ .] By requiring the two materials  $A$  and  $G$  to alternate, one considers in effect the joint distribution function  $P(A_n G_m)$  of one-dimensional “molecules”  $A_n G_m$ , rather than the individual  $p_\alpha$ . If the distribution functions  $p_A$  and  $p_G$  are uncorrelated, we have

$$P(A_n G_m) = p_A(n) p_G(m). \quad (1)$$

Sasaki *et al.*<sup>15</sup> chose this type of random sequence, with  $p_A(n) = p_G(n) = p(n)$ , for  $A = \text{AlAs}$  and  $G = \text{GaAs}$ . These authors chose  $p(n)$  to be nonzero only for a set of small integers, e.g.,  $p(1) = p(2) = p(3) = \frac{1}{3}$  and otherwise  $p(n) = 0$ . The form of Eq. (1) is also expected in SLs with unintentional random thickness fluctuations, if these fluctuations do not depend on the material deposition sequence (i.e., if there are no asymmetries of growing  $G$ -on- $A$  with respect to growing  $A$ -on- $G$ ).

Modifications of Eq. (1) have also been considered in intentionally disordered SLs. Chomette *et al.*<sup>14</sup> fixed the thickness of the AlAs segments to a constant  $n_0$ , hence,  $P(A_n G_m) = p_G(m) \delta(n - n_0)$ , (where  $n_0 \approx 10$ ), and  $p_G(m)$  was chosen to be a discrete Gaussian distribution around a mean thickness  $\langle m \rangle \approx 10$  ML. Arent *et al.*,<sup>45</sup> on the other hand, fixed the length  $M = n + m$  of each “molecule” using  $P(A_n G_{M-n}) = p(n)$ , where the distribution  $p(n)$  was chosen to be the same as that used by Sasaki *et al.*<sup>15</sup> In this approach  $p_A(n)$  and  $p_G(m)$  are completely correlated, since knowledge of one completely specifies the other. Therefore, in contrast to Sasaki *et al.*'s  $d$ -SL, Arent *et al.*'s variation corresponds to partially ordered SLs (po-SL), retaining long-range order.

The presence or absence of long-range order along the SL direction is conveniently measured in terms of the “layer-layer pair correlation function”  $\langle \Pi_2(i) \rangle$ . To calculate it, one assigns a pseudospin variable  $\hat{S}_i$  of value  $+1$  ( $-1$ ) if

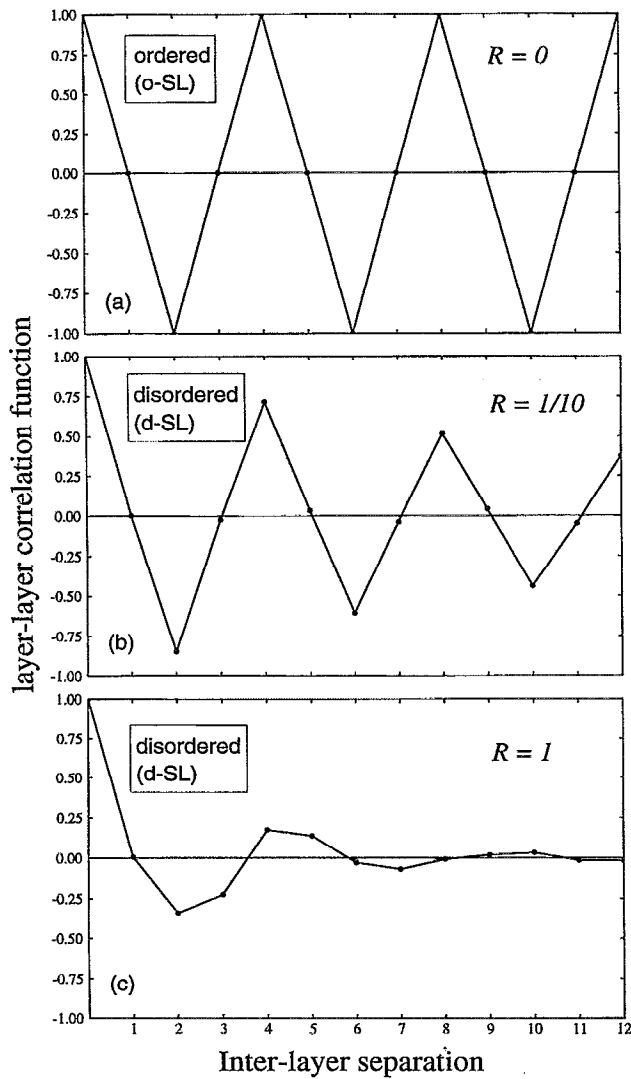


FIG. 2. Layer-layer correlation function  $\langle \Pi_2(j) \rangle$  [Eq. (2)] of (a) an ordered  $(A)_2/(G)_2$  superlattice (o-SL), (b) a disordered superlattice (d-SL) with a small degree  $R=1/10$  of thickness fluctuations [Eq. (3)], and (c) a d-SL with maximum disorder  $R=1$ .

monolayer  $i$  is occupied by material  $A(G)$ . The pair-correlation function for two monolayers separated by distance  $j$  is

$$\langle \Pi_2(j) \rangle = \left\langle \frac{1}{N} \sum_i^N \hat{S}_i \hat{S}_{i+j} \right\rangle, \quad (2)$$

where sum runs over the  $N$  monolayers of a particular realization of the SL, and the angular brackets denote a configurational average. In an ordered  $A_n/G_m$  SL we have in Eq. (2)  $N=n+m$  and  $\langle \Pi_2(j) \rangle$  is a periodic function with periodicity  $n+m$ . This is illustrated in Fig. 2(a) for an  $A_2/G_2$  o-SL, where  $\langle \Pi_2(j) \rangle$  is seen to be a (discrete) periodic function with amplitude unity and periodicity  $N=n+m=4$ . For a disordered SL, however, we must perform the configurational average in Eq. (2), or equivalently consider the limit  $N \rightarrow \infty$  of a particular realization of length  $N$ . Figure 2(b) shows  $\langle \Pi_2(j) \rangle$  of a d-SL with a small degree of disorder

[ $p(2)=\frac{5}{6}$  and  $p(1)=p(3)=\frac{1}{12}$ ], i.e., for a d-SL with average layer thicknesses  $\langle n \rangle=2$  corresponding to the exact layer thicknesses of the “parent” o-SL depicted in Fig. 2(a). Figure 2(c) shows the same quantity for a large degree of disorder, viz,  $p(1)=p(2)=p(3)=\frac{1}{3}$ . We see that  $\langle \Pi_2(j) \rangle$  decays much more rapidly than in Fig. 2(b), and its magnitude is less than 0.1 for  $j \geq 6$ .

In the special case of monolayer thickness fluctuations  $n'=n \pm 1$  around a given (ideal) layer thickness  $n$  we can define a single “order parameter”  $R$ . It is given by the relative frequency of the respective thickness fluctuations  $n+1$  and  $n-1$ , i.e.,

$$R = \frac{p(n+1)}{p(n)} = \frac{p(n-1)}{p(n)}. \quad (3)$$

Because the distribution  $p(n')$  is normalized, we can write  $p(n)=1/(1+2R)$  and  $p(n \pm 1)=R/(1+2R)$ . For the ideal, ordered  $n \times n$  superlattice  $R=0$ , and  $p(n')=\delta(n'-n)$ , whereas for a d-SL with  $R=1$  all three layer thicknesses  $\{n-1, n, n+1\}$  occur with equal probability  $p=\frac{1}{3}$ . The minimum value of  $R$  that can be reached in a SL of finite length  $N$  corresponds to a single “chain mutation,” (a single  $\delta$ -doped layer), and is  $R \approx 2n/N$ . In the following we often refer to this limiting case by the notation  $R \rightarrow 0$  (distinct from  $R=0$ ), since even in the limit  $N \rightarrow \infty$  the presence of a single thickness fluctuation should be distinguished from the ordered SL with  $R=0$ . To connect the parameter  $R$  to the more general Eq. (2), we plot in Fig. 2(b) the function  $\langle \Pi_2(j) \rangle$  of a d-SL with a small amount of thickness fluctuations  $R=\frac{1}{10}$  (i.e., one out of ten layers has a thickness of  $n+1$  or  $n-1$  ML, respectively). Indeed, the correlation function decays much more slowly than in the d-SL with  $R=1$  depicted in Fig. 2(c), and the “ideal” periodicity of 4 ML is still clearly discernible.

The one-dimensional Fourier transform of the real-space correlation functions of Eq. (2) equals  $|S(k_{\parallel})|^2$ , where  $k_{\parallel}$  is a wave vector along the SL direction. The form factor  $|S(k_{\parallel})|^2$  is proportional to the diffuse scattering intensity of a kinematic scattering experiment at zero temperature. Figure 3(a) shows  $|S(k_{\parallel})|^2$  of the ordered SL with correlation function  $\langle \Pi_2(j) \rangle$  depicted in Fig. 2(a), for  $k_{\parallel}$  lying in the first Brillouin zone of the empty linear chain. Clearly, the “diffuse scattering” of the o-SL consists of the new Bragg, or satellite peaks at  $k_{\parallel}=\frac{1}{4}, \frac{1}{2}, \frac{3}{4}$  of a linear chain with a unit cell four times as large as that of the empty chain. (The peak at  $k_{\parallel}=\frac{1}{2}$  vanishes because of the particular unit cell choice  $n=m=2$ .)  $|S(k_{\parallel})|^2$  of the d-SLs with  $R=\frac{1}{10}$  and  $R=1$  are shown in Figs. 3(b) and 3(c), respectively. The absence of long-range order leads to true diffuse scattering throughout the 1D Brillouin zone. The average periodicity  $\langle n \rangle + \langle m \rangle = 4$  still leaves fingerprints at the peak positions of the o-SL. (In the case  $R=1$ , there is also a maximum at the previously forbidden wave vector  $k_{\parallel}=\frac{1}{2}$ .)

In the special case of a partially ordered SL,<sup>45</sup> the layer-layer correlation function  $\langle \Pi_2(j) \rangle$  is periodic, but its amplitude is smaller than that of the ideal o-SL. Figure 4 shows  $\langle \Pi_2(j) \rangle$  for po-SLs with  $\langle n \rangle=2$ ,  $R=\frac{1}{10}$ , and  $R=1$  exhibiting clear long-range order without amplitude decay. The corresponding diffuse scattering (Fig. 5) is characterized by the

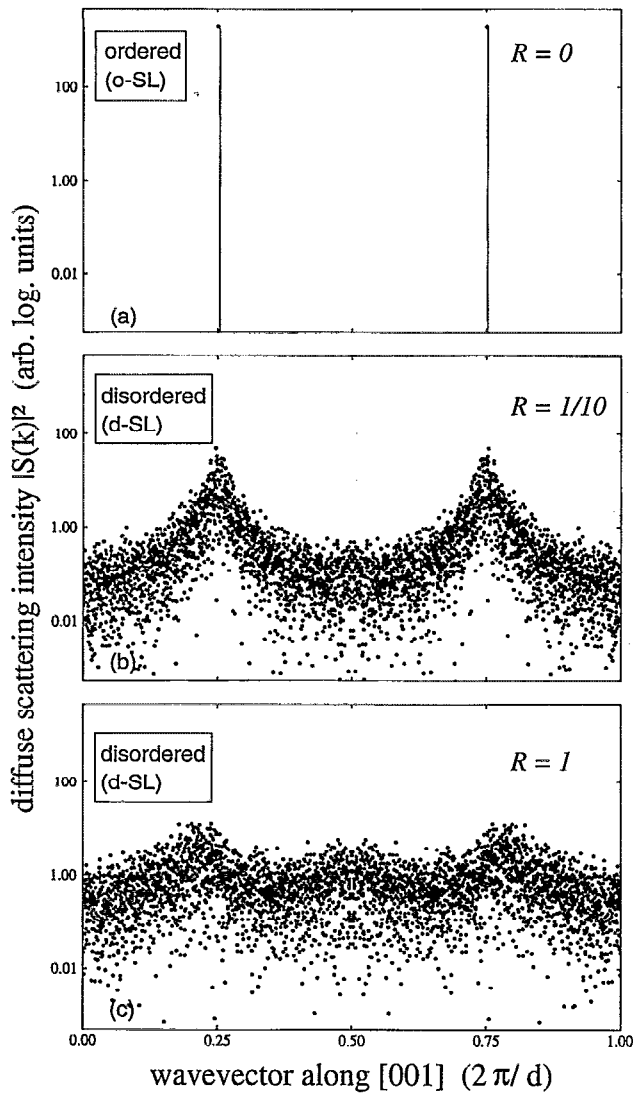


FIG. 3. The diffuse scattering intensities  $|S(k_{\parallel})|^2$  of the  $d$ -SLs shown in Figs. 2(a), 2(b), and 2(c), respectively.

coexistence of rather strong peaks at the  $o$ -SL peak positions (marked by vertical impulses) and a diffuse background of comparable amplitude than in a  $d$ -SL (Fig. 3).

The appearance of diffuse scattering intensity in a  $d$ -SL is in fact a manifestation of the relaxation of the  $k_{\parallel}$  selection rule due to the breaking of translational symmetry in the  $d$ -SL. We see in the following sections that the relaxation of the  $k_{\parallel}$ -selection rule has a profound effect also on the electronic structure of disordered superlattices.

### III. ELECTRONIC STRUCTURE CALCULATIONS

#### A. Three-dimensional pseudopotential representation of the electronic structure

##### 1. The pseudopotential and the basis set

Given the crystal structure of an ordered or disordered SL (Sec. II), we describe its electronic properties via the solution of

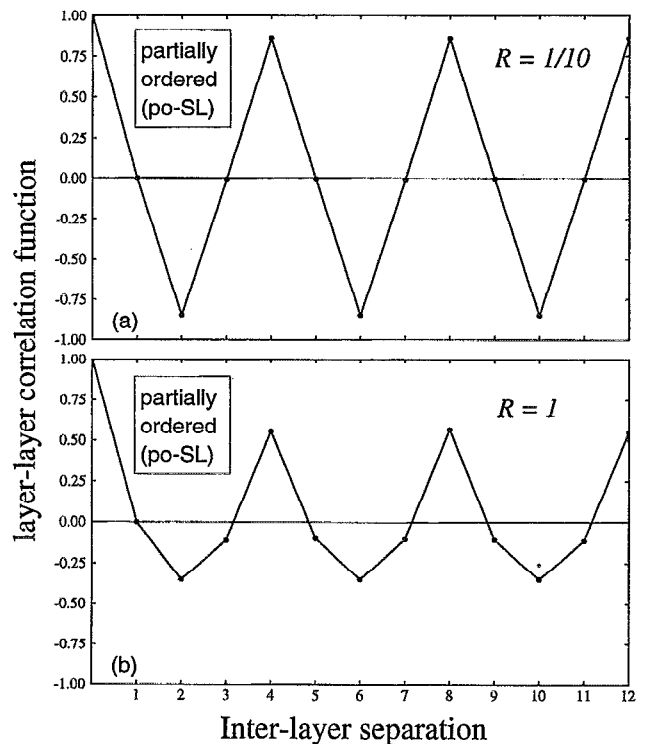


FIG. 4. Layer-layer correlation function  $\langle \Pi_2(j) \rangle$  [Eq. (2)] of a partially ordered superlattice (po-SL) with (a)  $R = 1/10$  and (b)  $R = 1$ .

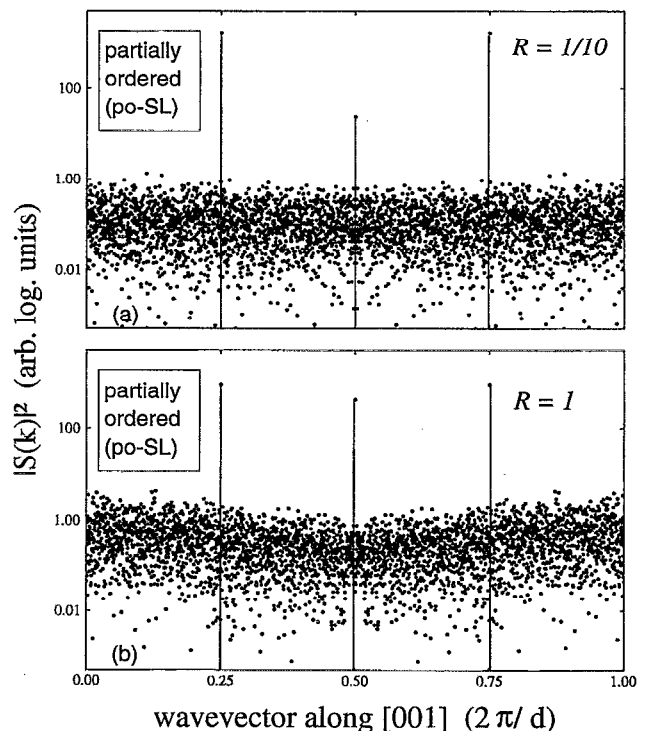


FIG. 5. The diffuse scattering intensities  $|S(k_{\parallel})|^2$  of the po-SLs shown in Figs. 4(a) and 4(b), respectively.

$$[-\frac{1}{2}\nabla^2 + V(x,y,z)]\psi_j(x,y,z,\mathbf{k}) = \epsilon_j(\mathbf{k})\psi_j(x,y,z,\mathbf{k}), \quad (4)$$

where  $V(x,y,z)$  is the three-dimensional screened local pseudopotential,

$$V(\mathbf{r}) = \sum_{\alpha} \sum_{R_n} v_{\alpha}(|\mathbf{r} - \boldsymbol{\tau}_{\alpha} - \mathbf{R}_n|), \quad (5)$$

constructed as a superposition over atom types  $\alpha$  and unit cells  $n$  of the screened atomic pseudopotentials  $v_{\alpha}(r)$ . We have recently parameterized  $v_{\alpha}(r)$  for  $\alpha = \text{Ga}, \text{Al}, \text{ and As}$ , so as to fit the experimentally measured band structures of bulk GaAs and AlAs (throughout the Brillouin zone), effective masses and deformation potentials, and the LDA calculated electronic wave functions of the short-period (GaAs)<sub>*n*</sub>/(AlAs)<sub>*n*</sub> superlattices. A detailed comparison of the bulk properties calculated with these empirical pseudopotentials and the experimentally observed properties is given in Ref. 48. An important aspect of this pseudopotential is that the arsenic potential depends on the identity of its four nearest neighbors, i.e., the number of Al and Ga atoms around it. This introduces important interfacial effects: the potential  $V(\mathbf{r})$  changes from GaAs-like to a mixed GaAlAs type at the interface and finally to AlAs-like. Thus, while  $V(\mathbf{r})$  is not calculated self-consistently, it was constrained to correctly describe LDA-calculated superlattices via introduction of such interfacial effects. This feature distinguishes our empirical pseudopotential calculations from other calculations of superlattices (see review of other calculations in Ref. 48).

Equation (4) is solved by expanding  $\psi_j(\mathbf{r},\mathbf{k})$  in plane waves,

$$\psi_j(\mathbf{r},\mathbf{k}) = \sum_{\mathbf{G}}^{G_{\max}} A_j(\mathbf{k},\mathbf{G}) e^{i(\mathbf{k}+\mathbf{G})\cdot\mathbf{r}}, \quad (6)$$

where  $\{\mathbf{G}\}$  are the reciprocal lattice vectors of the SL. The matrix elements of  $V(\mathbf{r})$  in the basis set of Eq. (6) are calculated by a Fourier transform, with no approximation except truncation: The basis set (6) is truncated at some maximum value of  $G_{\max} = 2.24$  a.u. (resulting in about 30 plane waves per atom in GaAs/AlAs systems) determined in the construction of the pseudopotential. Note that in Eqs. (4)–(6) we do not factor  $(x,y)$  from  $z$ ; instead, we treat the system as a real 3D problem. Note also that no use is made of effective-mass,  $k \cdot p$ , or envelope-function approximations here.

## 2. Solving the Schrödinger equation

Substitution of the plane-wave expansion of Eq. (6) into the Schrödinger equation Eq. (4) results in a matrix (secular) equation whose dimension is  $N_G \times N_G$ , where  $N_G$  is the number of plane waves entering Eq. (6). In practice, this number is related to the number of monolayers  $N = n + m + n' + m' + \dots$  in a unit cell. For an  $N$  monolayer SL with two atoms per monolayer the corresponding matrix dimension is about  $60N \times 60N$ ; typical  $d$ -SLs require  $N \sim 1000$  ML. Standard techniques for solving Schrödinger's equation require orthogonalization of each state to all other states, thus leading to an  $N_G^3$  scaling of the effort involved. This is impractical for  $N_G$  values ( $\sim 60\,000$ ) appropriate here. Fortunately, our physical interest lies only in the near-

gap levels, rather than in the many thousands of lower-lying energy levels. It was recently shown<sup>49</sup> that one could replace Eq. (4) by

$$[-\frac{1}{2}\nabla^2 + V(\mathbf{r}) - \epsilon_{\text{ref}}]\psi_j(\mathbf{r},\mathbf{k}) = (\epsilon_j - \epsilon_{\text{ref}})^2 \psi_j(\mathbf{r},\mathbf{k}), \quad (7)$$

where  $\epsilon_{\text{ref}}$  is an arbitrary “pointer” and  $\{\epsilon_j, \psi_j\}$  are identical to those appearing in Eq. (4). The lowest eigenvalue of Eq. (7) corresponds, however, to the eigenvalue closest to  $\epsilon_{\text{ref}}$ . Thus, by placing the “pointer”  $\epsilon_{\text{ref}}$  inside the band-gap region, one is guaranteed to find the valence-band maximum (VBM) or the conduction-band minimum (CBM). Since these are the lowest eigensolutions of Eq. (7), one does not spend any effort on orthogonalization. The total effort to find these states thus scales as  $N_G$ , rather than as  $N_G^3$ , so large problems can be solved readily. Reference 49 provides technical details on the preconditioned conjugate-gradient algorithm used to solve Eq. (7). The solutions of Eq. (7) obtained this way are *exact*, equalling those of Eq. (4).

## B. One-dimensional envelope-function model

In this subsection, we describe the effective-mass model used in addition to the pseudopotential method to calculate the electronic structure of the disordered SL. By using the effective mass model, we are able to find the eigenstates even far away from the band edge and obtain statistical properties of the states by calculating many different random sequences of the  $d$ -SL. Calculating the same quantities with the pseudopotential method would be very expensive.

Using the Kronig–Penney effective mass model, the three-dimensional problem of Eq. (4) is reduced to the one-dimensional problem

$$\left( -\frac{1}{2} \frac{d}{dz} \frac{1}{m^*(z)} \frac{d}{dz} + V_{\text{ext}}(z) \right) \phi_i(z) = \epsilon_i \phi_i(z). \quad (8)$$

Here  $m^*(z)$  is the effective mass,  $V_{\text{ext}}(z)$  is the external potential [to be distinguished from the microscopic atomic potential of Eqs. (4) and (5)], and  $\phi_i(z)$  is the envelope function.  $V_{\text{ext}}(z)$  is a constant within each material, as is the effective mass  $m^*(z)$ . Like in the empirical pseudopotential calculation, we assume periodic boundary conditions for the supercell. This is equivalent to connecting the left-hand end of the SL with its right-hand end. Written in the form of Eq. (8), we imply that the boundary condition at the GaAs/AlAs interface is the continuity of  $\phi_i(z)$  and  $m^*(z)^{-1} (d/dz) \phi_i(z)$ . More explicitly, we have

$$\left( m^{*-1} \frac{d\phi(z)}{dz} \right)_{\text{GaAs-IF}} = \left( m^{*-1} \frac{d\phi(z)}{dz} \right)_{\text{AlAs-IF}}, \quad (9)$$

where IF denotes interface.

Equation (8) can be solved using a transfer matrix technique,<sup>50</sup> taking advantage of the fact that within each layer both  $m^*$  and  $V_{\text{ext}}$  are constants. Let us denote by  $l$  the layer index ( $l = 1, \dots, N$ , running from left- to right-hand side). Then,  $m_l^*$ ,  $V_l$ , and the layer length  $d_l$  specify the physical property of the  $l$ th layer. If we define a two-variable array  $A_l$  as

$$A_l = \begin{pmatrix} \phi(z_l) \\ \frac{1}{m_l^*} \frac{d}{dz} \phi(z_l) \end{pmatrix} \quad (10)$$

(where  $z_l$  is the left-hand-side position of the  $l$ th layer), then from Eq. (8)  $A_{l+1}$  is given by

$$A_{l+1} = M_l(E)A_l, \quad (11)$$

where  $E$  is the energy of the wave function. Transfer matrix  $M_l(E)$  is defined as follows.

For  $E \geq V_l$  and  $k = \sqrt{2m_l^*(E - V_l)}$ , we have

$$M_l(E) = \begin{pmatrix} \cos(kd_l) & \sin(kd_l)/k \\ -km_{l+1}^* \sin(kd_l)/m_l^* & m_{l+1}^* \cos(kd_l)/m_l^* \end{pmatrix}, \quad (12)$$

while for  $E < V_l$  and  $k = \sqrt{2m_l^*(V_l - E)}$  we have

$$M_l(E) = \begin{pmatrix} \cosh(kd_l) & \sinh(kd_l)/k \\ km_{l+1}^* \sinh(kd_l)/m_l^* & m_{l+1}^* \cosh(kd_l)/m_l^* \end{pmatrix}. \quad (13)$$

To solve for an eigenstate  $\phi_i(z)$  and an eigenvalue  $\epsilon_i$  of the  $N$ -layer SL, we require that the wave function satisfy the periodic condition

$$A_{N+1} = \left( \prod_{l=1}^N M_l(E) \right) A_1 = A_1. \quad (14)$$

The  $i$ th solution of  $E$  yields  $\epsilon_i$  whereas the  $i$ th solution of  $A_i$  yields  $\phi_i(z)$ .

To solve Eq. (14), we calculate the determinant

$$d(E) = \det \left( \prod_{l=1}^N M_l(E) - 1 \right), \quad (15)$$

and scan  $d(E)$  within the interesting range of  $E$ . A change of sign in  $d(E)$  when  $E$  increases indicates a solution. Then Newton's iteration method is used to find the exact  $E$  value which yields the zero of  $d(E)$ . However, for the  $d$ -SL, when  $E$  is close to the band edge, this procedure is numerically unstable for large  $N$  due to the typical exponential growth of  $\prod_{l=1}^N M_l(E)$  as a function of  $N$ . In this case, we need another procedure to find localized states. We start with  $A_1 = [0, 1]$  and scan  $A_{N+1}(E) = [a(E), b(E)]$  as a function of  $E$ . Then  $a(E) = 0$  gives the eigenvalue of a localized state. However, if  $\phi(z_l)$  belonging to this  $E$  has large amplitude near  $l=1$  or near  $l=N$ , then the eigenenergy of this state has to be recalculated by shifting the starting (the ending) position from  $l=1$  ( $l=N$ ) to another point, so that this localized state is in the middle of the starting and ending points.

By switching between the above two procedures, we can reliably calculate all the states of a one-dimensional system for almost arbitrarily large  $N$ .

To solve the 1D problem we need to determine the external potential  $V_{\text{ext}}$  (i.e., band lineups) and effective masses. The EPM calculated band offsets at the GaAs/AlAs interface are given in Fig. 6. Since the AlAs  $X_{1c}$  state is near the CBM, for small period superlattice, the  $X$  valley derived electron state could be important. For large period superlattices, the absolute CBM is the GaAs  $\Gamma_{1c}$  state, thus  $\Gamma$  valley derived electron states are important. Thus, for electron

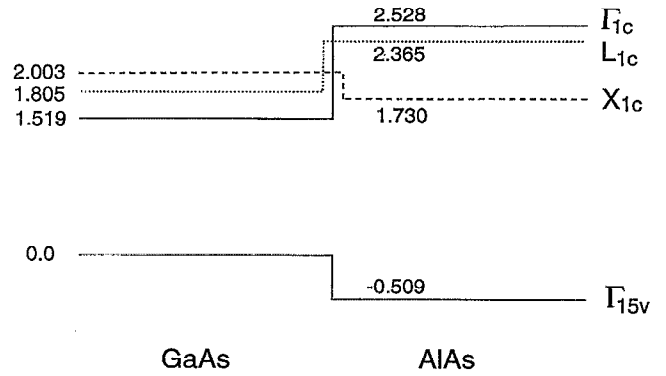


FIG. 6. Band offsets (eV) used for the GaAs/AlAs interface. These band-edge energies yield their corresponding potential  $V(z)$  in the effective-mass calculation of Eq. (8).

states, we calculate states derived from  $\Gamma$  and  $X$  valleys. The  $L$  valley derived states is also calculated in some cases to compare with the pseudopotential results. For holes we only calculate  $\Gamma$  valley derived heavy-hole states.

The effective masses calculated from the empirical pseudopotential for the (001) and (111) directions using  $m^* \approx \Delta k^2 / 2\Delta E$  are shown in Table I. Using the band offsets of Fig. 6 and the masses given in Table I, we can calculate the electronic structure of superlattices using the EMA of Eq. (8).

#### IV. RESULTS

In this section, we discuss the following cases:

- The ideal ordered superlattice of period  $n$ . Here  $R \equiv 0$  and  $p(n') = \delta(n' - n)$ . This will establish the electronic structure of our "unperturbed system" (Sec. IV A);

TABLE I. EPM effective masses (in units of free electron mass) at different valleys along different directions. The GaAs  $X$  valley energy minimum is at  $(0.89, 0, 0)(2\pi/a)$ , where  $a$  is the lattice constant. Its effective mass is evaluated at this energy minimum point. All other valley minima are at their corresponding high-symmetry  $\mathbf{k}$  points.

	$\Gamma$ valley: (000)		
	Heavy hole	Light hole	Electron
GaAs (100)	0.416	0.079	0.077
GaAs (111)	0.975	0.065	0.077
AlAs (100)	0.439	0.157	0.158
AlAs (111)	1.020	0.111	0.158
	$X$ valley: (100)		
	Parallel: [100]	Perpendicular: [010]	Along [111]
	GaAs	1.912	0.246
AlAs	2.194	0.262	0.371
	$L$ valley: $\frac{1}{2}(111)$		
	Parallel: [111]	Perpendicular: $[\bar{2}11]$	Along [100]
	GaAs	1.664	0.128
AlAs	2.120	0.168	0.242

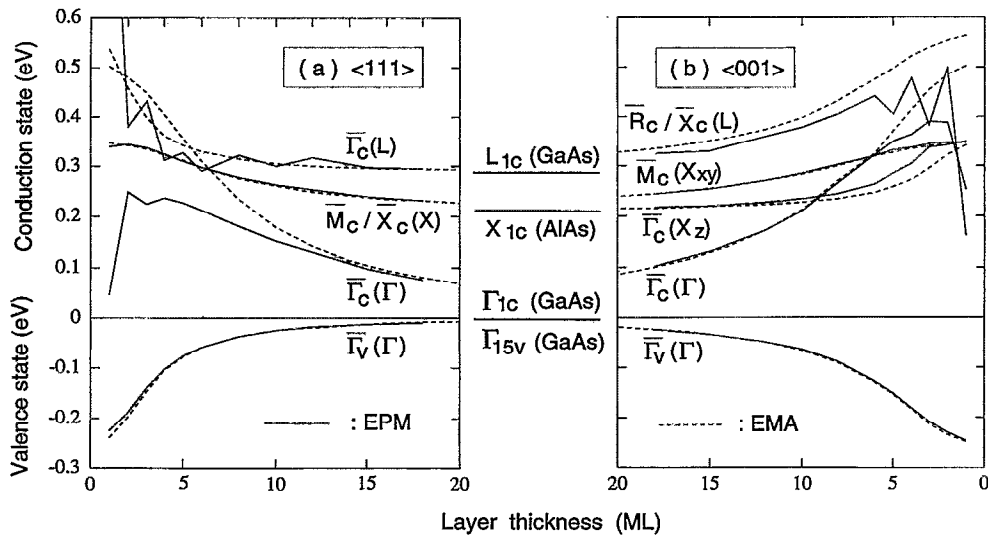


FIG. 7. Energy levels of ideal  $(\text{AlAs})_n/(\text{GaAs})_n$  superlattices along (a)  $\langle 111 \rangle$  and (b)  $\langle 001 \rangle$ , as a function of period  $n$ . Solid lines: pseudopotential results; dashed lines: effective-mass results. The bulk levels in the middle column are reached asymptotically as  $n \rightarrow \infty$ . The SL states are denoted with an over bar, while their parent zinc-blende states  $\Gamma$ ,  $X$ , and  $L$  are given in parentheses.

- (b) SLs with laterally intermixed interfaces. Here, the  $(x,y)$ -averaged composition profile is periodic along  $z$  (Sec. IV B);
- (c) The single  $\delta$ -doping layer case. Here, a monolayer of AlAs or GaAs embedded in a perfectly ordered SL. This will establish the existence of bound states due to the chemical disparity between the  $\delta$  layer and the host SL (Sec. IV C);
- (d) An ordered array of interacting  $\delta$  layers. Here, starting from the single  $\delta$  layer with  $R \rightarrow 0$  one reduces the fixed separation between the  $\delta$  layers, thus increasing<sup>51</sup>  $R$ . This case will establish the electronic structure of the chemically perturbed system without any disorder (Sec. IV D); finally, we consider
- (e) Random arrays of interacting  $\delta$  layers. Here  $0 < R \leq 1$ . This system has both chemical perturbations and substitutional randomness, and includes the disordered SLs considered by Sasaki *et al.*,<sup>15</sup> and the partially ordered ones by Arent *et al.*<sup>45</sup> (Sec. IV E).

### A. Ideal periodic AlAs/GaAs superlattices: Abrupt interfaces

The solid lines in Fig. 7 depict the dependence of the pseudopotential-calculated high-symmetry superlattice energy levels on the period  $n$ , for (001)- and (111)-oriented SLs. The results correspond to the scalar-relativistic limit without spin-orbit interaction. Since we do not use envelope functions, the results are not limited to near zone center states. We show in fact the  $\Gamma$ -folded (denoted  $\bar{\Gamma}$ ),  $X$ -folded (denoted  $\bar{M}$  or  $\bar{X}$ ), and  $L$ -folded (denoted  $\bar{R}$  or  $\bar{X}$ ) states. In agreement with previous theoretical LDA studies,<sup>52</sup> we find the following for the (111) SL [Fig. 7(a)]:

(i) The ideal SL has a direct band gap for all  $n$  values, since the conduction-band minimum is the  $\Gamma$ -folded  $\bar{\Gamma}_{1c}(\Gamma_{1c})$  state. This SL has a “type-I” band arrangement for

all period  $n$ . Both the highest valence and the lowest conduction states are localized on the GaAs layers.

(ii) The second conduction band at  $\Gamma$ , i.e.,  $\bar{\Gamma}(L)$ , is folded from the zinc-blende  $\bar{\Gamma}-L_z$  line. For small  $n$ , this pseudodirect  $\bar{\Gamma}_c(L_c)$  state mixes strongly with the direct  $\bar{\Gamma}_c(\Gamma_c)$  state. The mixing, and thus the level repulsion, shows odd-even energy oscillations for small  $n$  (reflecting localization of repelling states on the same or on either sublattice<sup>52</sup>).

(iii) For  $n > 6$  the  $X$ -folded, indirect  $\bar{M}_c(X_c)$  conduction state lies below the pseudodirect,  $\bar{\Gamma}_c(L_c)$  state. The SL states asymptotically approach their respective bulk values (see middle column of Fig. 7).

The situation is very different for (001)-oriented ideal SLs. The prominent properties apparent in Fig. 7(b) are:

- (i) The  $n=1$  SL has an indirect band gap at the  $L$ -folded point<sup>52,53</sup>  $\bar{R}$ ;
- (ii) For  $n < 4$ , the lateral  $X_{x,y}$  valleys (folded to  $\bar{M}$ ) and the  $X_z$  valley (folded to  $\bar{\Gamma}$ ) are nearly degenerate;<sup>54</sup>
- (iii) For  $1 < n \leq 8$  the pseudodirect, AlAs-like  $\bar{\Gamma}_c(X_z)$  state is below the direct, GaAs-like  $\bar{\Gamma}_c(\Gamma_c)$  state, thus the SL is type II;<sup>55</sup> for  $n > 8$ , however,  $\bar{\Gamma}_c(\Gamma_c)$  is lower, so the system is type I (experimentally, the type-II/type-I crossover is found<sup>54</sup> at  $n \approx 11$ ).

The effective mass energies of (001) and (111) SLs are compared in Fig. 7 (dashed lines) with the EPM results (solid lines). The effective masses used in the EMA are from Table I which is calculated from the EPM. At large superlattice period  $n$ , the EMA results agree very well with the EPM results. [For the (001)  $\bar{R}/\bar{X}(L)$  curve, there is a small discrepancy]. For  $\bar{\Gamma}_v(\Gamma)$  and  $\bar{M}_c/\bar{X}_c(X)$ , we find good agreement with EPM results even down to  $n=1$ . This is because

- (i) for  $\bar{M}_c(X_{xy})$  (001) and  $\bar{M}_c/\bar{X}_c(X)$  (111) states, there is no mixing between states from different valleys;<sup>52</sup>
- (ii) unlike the cases in 2D and 3D systems, in 1D systems the heavy hole does not mix with the light-hole states;

- (iii) the potential offsets for the GaAs/AlAs interface are small (Fig. 6), thus, even for  $n=1$ , the  $k$  in Eqs. (12) and (13) is small, so nonparabolicity is small.

In contrast to the good agreement between EMA and EPM for the above states, the EPM  $\bar{\Gamma}_c(\Gamma)$  curve for both (001) and (111) bends down at small  $n$ , while in the EMA there is a monotonic dependence. The EPM bending is due to the mixing of  $\bar{\Gamma}_c(\Gamma)$  with  $\bar{\Gamma}_c(X_z)$  in the (001) case and with  $\bar{\Gamma}_c(L)$  in the (111) case.<sup>52</sup> This cannot be described by the one-band effective mass model (or even four-band  $k \cdot p$  model<sup>56</sup>). The large oscillations in the EPM results for  $\bar{R}_c \bar{X}_c(L)$  (001) and for  $\bar{\Gamma}_c(L)$  (111) (also due to mixing) cannot be described by a one-band EMA model (or a four-band  $k \cdot p$  model<sup>56</sup>), either.

## B. Periodic AlAs/GaAs superlattices: Laterally intermixed interfaces

### 1. Intermixing in (001) superlattices

Chemical nonabruptness of interfaces in short-period superlattices has been suggested by Laks and Zunger<sup>57</sup> as a reason for the discrepancy between the experimental assignment of the conduction-band minimum and theoretical predictions. In particular, for the monolayer ( $n=1$ ) superlattice along (001), our calculation [Fig. 7(b)] places the conduction-band minimum at the  $L$ -derived  $\bar{R}$  point in the tetragonal Brillouin zone,<sup>58</sup> whereas experimentally a  $X_{x,y}$ -derived gap at  $\bar{M}$  is found.<sup>54</sup> We tested the idea of Laks and Zunger<sup>57</sup> using intermixed interfaces. The monolayer superlattice can be viewed as a partially ordered structure, i.e., it can be written as

$$(\text{Al}_{1/2+\eta/2}\text{Ga}_{1/2-\eta/2}\text{As})_1 (\text{Al}_{1/2-\eta/2}\text{Ga}_{1/2+\eta/2}\text{As})_1,$$

where  $\eta$  is the long-range-order (LRO) parameter.  $\eta=1$  denotes the ideal superlattice with abrupt interfaces, whereas  $\eta=0$  characterizes the random alloy. To simulate interfacial roughness in the monolayer superlattice we expand the repeat period ( $X \times Y$ ) in the interface plane to an  $(8 \times 8)$  unit cell. We can thus have  $\eta=1-n/32$ , where  $n$  is the number of Ga/Al pairs interchanged across the interface. In each cation layer, the Ga and Al atoms are randomly distributed on the lattice sites, hence, microscopically the interfacial roughness pattern does not repeat itself from one interface to the next interface. As a result, there is in principle no periodicity even along the growth axis [001]. For computational reasons, however, we assume a repeat period of 4 ML along [001], resulting in a 512 atom supercell. Hence, within the supercell there are four distinct Al-rich and four distinct Ga-rich layers, with compositions  $0.5+\eta/2$  and  $0.5-\eta/2$ , respectively.

The energy eigenvalues of the large supercell are analyzed in terms of their "parent" zinc-blende states from which they originate. Because zinc-blende states are allowed to mix in the superlattice (subject to  $k$  selection and point-group selection rules), a superlattice wave function can be expanded in terms of a usually small number of zinc-blende wave functions. We use the expansion coefficients of the latter expansion as weights in evaluating spectral averages of zinc-blende-like eigenvalues.<sup>59</sup> For example,  $\langle \Gamma_{1c} \rangle$  denotes the expectation value of the zinc-blende  $\Gamma_{1c}$  energy level in a

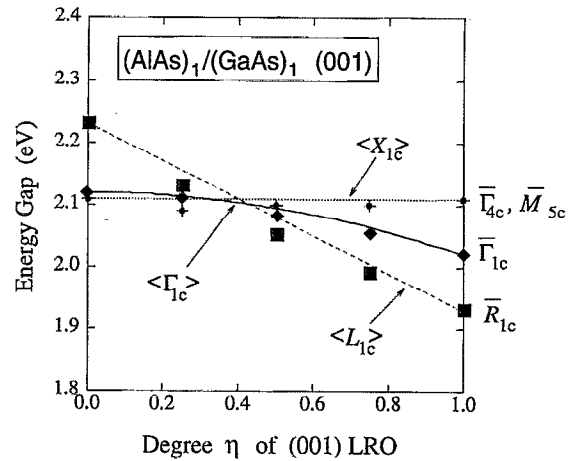


FIG. 8. Pseudopotential calculated spectral averages of the zinc-blende-like  $\Gamma_{1c}$  (diamonds),  $X_{1c}$  (pluses), and  $L_{1c}$  (squares) energy gaps, respectively, plotted as a function of  $\eta$ , the degree of (001) long-range order. The solid line is a quadratic interpolation between the  $\eta=0$  and  $\eta=1$  values of  $\langle \Gamma_{1c} \rangle$  and the broken lines are linear interpolations between the respective end points of  $\langle X_{1c} \rangle$  and  $\langle L_{1c} \rangle$ .

given supercell.  $\langle \Gamma_{1c} \rangle$ ,  $\langle X_{1c} \rangle$ , and  $\langle L_{1c} \rangle$  are shown in Fig. 8 for  $\eta=0, 0.25, 0.50, 0.75$ , and for the perfect monolayer superlattice ( $\eta=1$ ). Interpolation curves based on simple scaling laws<sup>37</sup> pertinent to LRO are shown as lines. We predict a transition from an  $X$ -like CBM to an  $L$ -like CBM at  $\eta \approx 0.4$ , in close agreement with the LDA result<sup>57</sup> ( $\eta \approx \frac{1}{2}$ ). Thus, our calculated result agrees with the experimental observation<sup>54</sup> if  $\eta < 0.4$  in the studied samples.

### 2. Intermixing in (111) superlattices

As the repeat period  $n$  of the ideal SL increases, chemical intermixing across the interface should have a decreasing impact on the band structure. Nevertheless, even for  $n=6$  the band gaps can shift considerably. We have considered the  $(\text{AlAs})_n/(\text{GaAs})_6$  (111) SL, because of a controversy about the nature of the band gap between theory<sup>52,60</sup> and experiment.<sup>61</sup> Cingolani and co-workers<sup>61</sup> concluded from their photoluminescence experiments that the  $n=6$  SL had an indirect band gap, i.e., a type-II alignment, whereas theory<sup>52,60</sup> predicts a direct band gap if the interfaces are abrupt [see Fig. 7(a)]. To test the effect of interfacial intermixing on the nature (direct versus indirect) of this SL, we have used a planar  $(4 \times 4)$  unit cell to simulate chemical intermixing within  $\pm 1$  ML across the interfaces, resulting in a 384 atom 3D unit cell. The superlattice is thus converted into a sequence of four GaAs layers, two alloy layers, four AlAs layers, and two alloy layers. We chose the composition of the alloy layers to be 50%, corresponding to maximum intermixing. Table II compares the band gaps of the intermixed SL with those in the ideal SL. We find that the direct band gap (folded from  $\Gamma_{6c}$ ) is blue shifted by 80 meV, while the pseudodirect  $\bar{\Gamma}_{6c}(L_{6c})$  and indirect gaps  $\bar{M}_{6c}(X_{6c})$  are blue shifted by 20–50 meV. The lowest transition, however, does not change upon intermixing, remaining  $\bar{\Gamma}_{6c}(\Gamma_{6c})$  although the pseudodirect transition  $\bar{\Gamma}_{6c}(L_{6c})$  is now only 20 meV (down from 50 meV) away.

TABLE II. Band gaps (in eV) of the  $(\text{AlAs})_c/(\text{GaAs})_6$  (111) superlattice with ideal and chemically intermixed interfaces. The zinc-blende (ZB) parent states are found by projecting the SL wave functions on ZB states.

Gap (ZB origin)	Ideal SL	Intermixed
$\bar{\Gamma}_{6c}(\Gamma_{6c})$	1.81	1.89
$\bar{\Gamma}_{6c}(L_{6c})$	1.86	1.91
$\bar{M}_{6c}(X_{6c})$	1.92	1.95
$\bar{M}_{6c}(L_{6c})$	2.02	2.04

Experimentally, the absorption edge was determined to be at 1.90 eV,<sup>61</sup> close to our calculated band gap of the intermixed SL. The observed PL emission peak at 1.80 eV, however, cannot be explained by chemical intermixing: Table II shows that intermixing leads to a blue shift while experimentally the PL is red shifted. A possible explanation for a large red shift of the PL emission is offered in Sec. IV E, where it is shown that monolayer thickness fluctuations lead to a red shift.

### C. A single $\delta$ layer inside an ordered superlattice

We next model the case of a single layer of  $A$  or  $G$  inserted in an ordered  $A_2/G_2$  SL. It is well known<sup>62</sup> that, while in 3D an impurity potential has to exceed a certain threshold value in order to create a localized gap level, in 1D, an attractive  $\delta$  potential of any magnitude always has a bound state. To understand the possibility of impuritylike localization, consider, for example, a  $G_3$   $\delta$  layer embedded in the otherwise perfect  $o$ -SL  $\cdots A_2 G_2 A_2 G_2 A_2 G_2 \cdots$ , thus converting it into  $\cdots A_2 G_2 A_2 G_3 A_2 G_2 \cdots$ , denoted as  $A_2/G_2:G_3$ . If the  $G_3$   $\delta$  layer is attractive to electrons (holes) it will bind a state below the CBM (above the VBM) of the  $o$ -SL.<sup>63</sup> We find that a  $(\text{GaAs})_3$   $\delta$  layer in the  $(\text{AlAs})_2/(\text{GaAs})_2$   $o$ -SL indeed binds an electron and a (double degenerate) hole [Fig. 9(a)], while an  $(\text{AlAs})_3$  layer binds an electron but does not bind a hole (Fig. 10). Figure 11 shows as dashed lines the dispersion of the bound states of a single  $\delta$  layer in  $A_2/G_2$ . The thin solid lines denote the dispersion of the energy bands of the  $n=2$  ordered SL along the symmetry lines  $\bar{\Sigma}$  and  $\bar{\Delta}$ , i.e., from  $\bar{\Gamma}$  to  $\bar{M}=1/\sqrt{2}(1,1)$  and from  $\bar{\Gamma}$  to  $\bar{X}=1/\sqrt{2}(1,0)$ , respectively. The thin horizontal lines denote the band edges of the  $o$ -SL: We see that the  $n=2$   $o$ -SL has a CBM at  $\bar{M}$  (2.09 eV above the VBM), and a VBM at  $\bar{\Gamma}$  at  $E=0$ . Any state of the perturbed SL that falls between these states will therefore correspond to a "bound state." For the  $\delta$  layer, we see no bound state at  $\bar{X}$  but the electron binding energies of  $A_2/G_2:G_3$  at  $\bar{\Gamma}$  and  $\bar{M}$  are  $\Delta\varepsilon_e=17$  and 4 meV, respectively, while those of  $A_2/G_2:A_3$  are  $\Delta\varepsilon_e=33$  and 5 meV, respectively. The hole binding energy of  $A_2/G_2:G_3$  is  $\Delta\varepsilon_h=37$  meV.

All other states for single  $\delta$ -layer doping in  $(\text{GaAs})_2/(\text{AlAs})_2$  are extended states, as illustrated in Fig. 9(b) for the next higher (lower) state following the bound electron (hole) in  $A_2/G_2:G_3$ .

The wave-function localization perpendicular to the  $\delta$ -layer plane is conveniently quantified in terms of the fol-

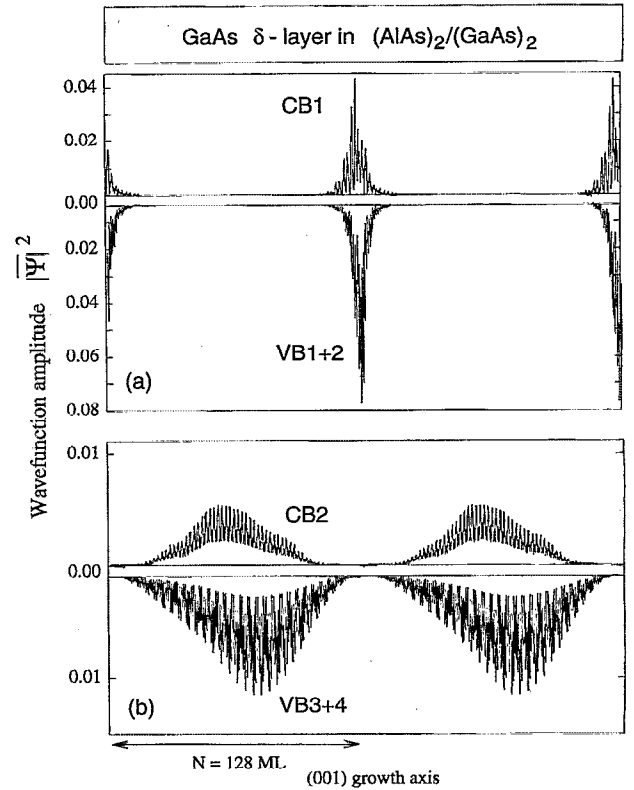


FIG. 9. Pseudopotential calculated planar average of the wave functions squared in an  $o$ -SL host containing a single  $(\text{GaAs})_3$   $\delta$  layer. Occupied states are plotted in the negative direction with a small offset for clarity. (a) Shows the  $\delta$ -layer bound states, (b) shows the first extended states.

lowing length scales (in ML units). The effective localization length for wave function  $\psi_E$  at energy  $E$  is defined as<sup>64</sup>

$$L_{\text{eff}}(E) = \frac{1}{d} \left[ \int dz \left( \int dx dy |\psi_E(\mathbf{r})|^2 \right)^2 \right]^{-1}, \quad (16)$$

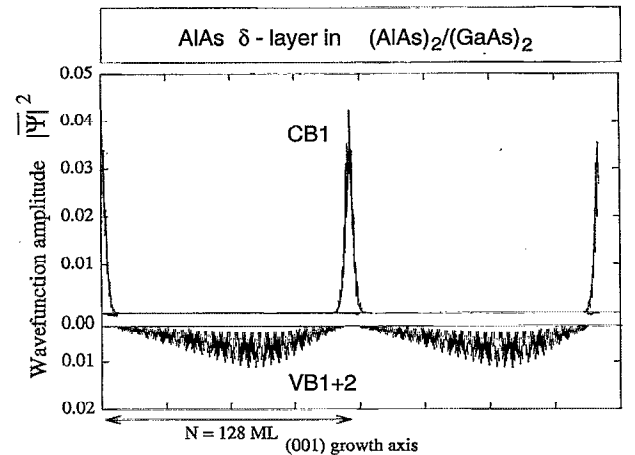


FIG. 10. Like Fig. 9, but for an  $(\text{AlAs})_3$   $\delta$  layer. In this case, there is no bound hole state.

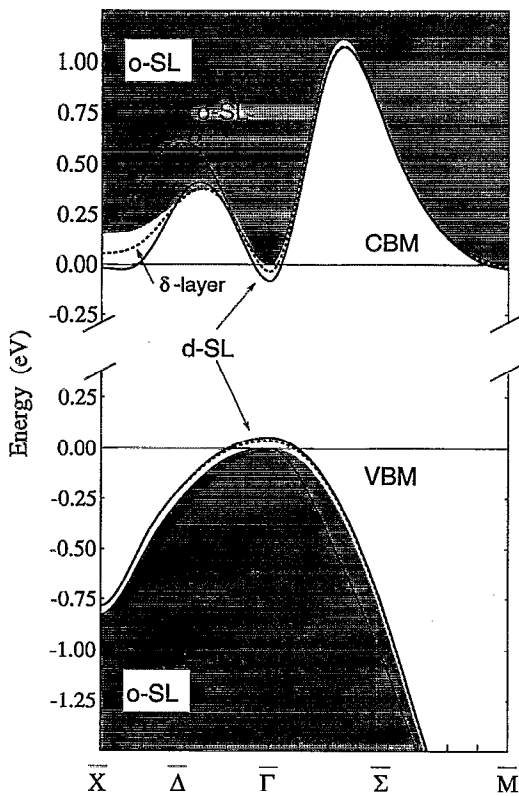


FIG. 11. Pseudopotential calculated dispersion of the band-edge state in a  $d$ -SL (solid lines),  $o$ -SL (thin lines), and a single  $\delta$  layer in an  $o$ -SL host (dotted lines) along the  $\bar{\Delta}$  and  $\bar{\Sigma}$  symmetry lines in the planar Brillouin zone. Also shown are the (001)-projected bands of the  $o$ -SL (shaded area). The supercell size is  $N=128$ .

and measures the region along  $z$  where  $\psi_E$  is “sizeable.” In Eq. (16) the planar average of  $|\psi_E|^2$  is taken before integrating along  $z$ ,  $d$  is the monolayer thickness, and the wave function is assumed to be normalized in the volume of the supercell. It is easy to see that an extended state has  $L_{\text{eff}} \sim N$ , whereas a state that is completely confined to one monolayer has  $L_{\text{eff}}=1$ . The asymptotic decay length  $\gamma^{-1}$  far away from the localization region is given by  $\langle |\psi_E(z)| \rangle \propto e^{-\gamma z}$ , where the angular brackets denote averaging over the fast oscillations of the planar average  $|\psi_E(z)|$  along  $z$ . The bound-state localization lengths  $\gamma^{-1}$  and  $L_{\text{eff}}$  obtained with a single  $\delta$  layer are given in Table III. We see that these values are

TABLE III. Effective localization length  $L_{\text{eff}}$  [Eq. (16)] and exponential decay length  $\gamma^{-1}$  for the  $\delta$ -layer systems depicted in Figs. 9 and 10, and the disordered and partially ordered SLs depicted in Figs. 15 and 16, respectively. Reported are the values for the states at the conduction-band minimum (CBM) and at the valence-band maximum (VBM) in ML units.

	CBM		VBM	
	$L_{\text{eff}}$	$\gamma^{-1}$	$L_{\text{eff}}$	$\gamma^{-1}$
$A_2/G_2:G$	11	5.0	10	5.0
$A_2/G_2:A$	7	2.9	$N$	...
$d$ -SL	14	4.8	12	4.3
po-SL	18	5.0	12	3.3

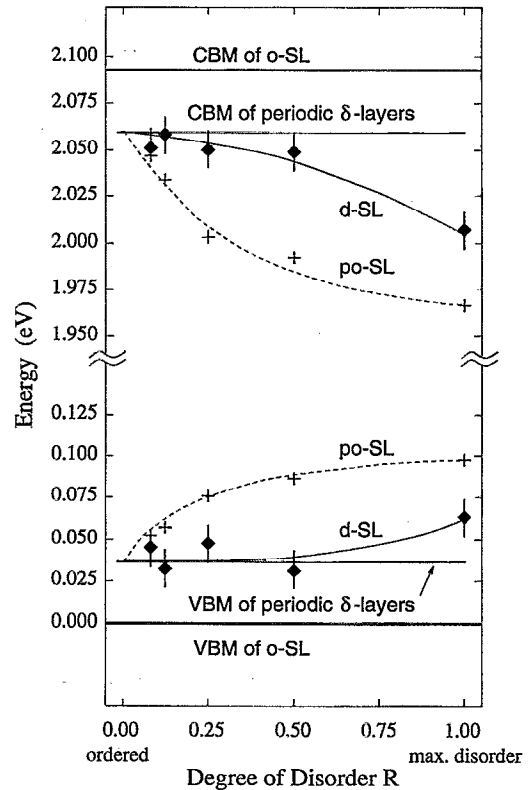


FIG. 12. Pseudopotential calculated band-edge energies of disordered ( $d$ -SL, diamonds), partially ordered superlattices (po-SL, pluses), and a periodic array of  $\delta$  layers embedded in an  $o$ -SL (thin horizontal lines) as a function of  $R$  [Eq. (3)]. Lines are guides to the eye. The thick horizontal lines denote the unperturbed band edges of the parent  $o$ -SL. The vertical bars on the  $d$ -SL data points denote the range of binding energies obtained from  $\sim 10$  different realizations of a  $d$ -SL with length  $N=128$ .

similar to those obtained in the fully disordered SL, suggesting that the same mechanism of localization could be at work in both cases.

#### D. An ordered array of $\delta$ layers inside an ordered superlattice

As one increases the density of the  $\delta$  layers inside the  $o$ -SL  $A_2G_2$ , these layers start to interact. As a first step, we arrange the  $\delta$  layers periodically, i.e., without any disorder. The density of  $\delta$  layers is proportional to  $R$  defined in<sup>51</sup> Eq. (3). The calculated energies as a function of  $R$  are depicted as the thin solid line in Fig. 12. We see that even for an array of closely spaced  $\delta$  layers ( $R \rightarrow 1$ ) the binding energy does not increase, indicating negligible interaction between the neighboring, coherently arranged bound states. In fact, at  $R=1$  the SL sequence consists of one layer of each thickness  $n=1, 2, 3$ , e.g.,  $G_3A_2G_1A_3G_2A_1$ , which is repeated periodically. Since the repeat period is only  $N=12$  ML, this structure is too short to describe a localized state bound to one  $\delta$  layer (see Fig. 9), which has a localization length  $L_{\text{eff}} \approx 10$ . The energy eigenstates and eigenvalues are thus those of a new superstructure with a complex unit cell, rather than those of a disordered system. Consequently, short supercells

TABLE IV. Overview of different disordered systems [superlattices (SL) and multiple quantum wells (MQW)] in the parameter space of  $R$  [Eq. (3)] and  $\Delta n/n$ .

	Small mean density ( $R \ll 1$ )	Large mean density ( $R \approx 1$ )
Small fluctuation ( $\Delta n \ll n$ ) $n \geq 10$	nearly "ideal" SL/MQW impuritylike localized states local level in gap	strongly disordered MQW effective-mass-like bound states discrete spectrum with QW-like quantum numbers
Large fluctuation ( $\Delta n \approx n$ ) $n < 10$	Strong perturbation of band edges Band-gap pinning	$d$ -SL, po-SL Band tail of localized states

with  $N \approx 10$ – $20$ , as have been used before to describe disordered SLs,<sup>39</sup> are unable to simulate the behavior of truly disordered SLs.

### E. A disordered array of $\delta$ layers

Next, we introduce disorder in the SL by arranging the  $\delta$  layers in the  $o$ -SL host at random. We have shown in Sec. II that very large supercells are required, if one wishes to accurately describe the layer–layer correlation function of a disordered system. We have used total lengths  $N$  of up to 1000 ML for EPM, and up to 2000 ML for EMA calculations, in order to verify the convergence of the results obtained with smaller supercells (typically  $N \approx 100$ – $250$ ). In principle, a configurational average of the properties of interest needs to be evaluated; in some cases (see below) we have used  $\sim 10$  realizations of a  $d$ -SL of given total length  $N$  and disorder parameter  $R$ , and have found that the EPM-calculated quantities of interest (band gap, localization lengths) have very small fluctuations. Therefore, we have often used a single realization of a  $d$ -SL to calculate band-edge energies and wave functions. For the EMA-calculated density of states, on the other hand, we have performed configurational averages over 100 realizations of a  $d$ -SL.

In the following, we discuss separately two regimes of thickness fluctuations. First, we consider the case where the thickness fluctuations  $\Delta n$  are of the same order as the unperturbed thickness, i.e.,  $\Delta n \approx n$ . This case includes the  $d$ -SLs of Sasaki *et al.*<sup>15</sup> and the po-SLs of Arent *et al.*<sup>45</sup> Second, we treat the case where the thickness fluctuations are relatively small perturbations of the ideal SL, i.e.,  $\Delta n \ll n$ . An overview of the different regimes considered is given in Table IV.

#### 1. Disordered SLs with $\Delta n \approx n$ : EMA density of states

To calculate the spectral properties of a  $d$ -SL over a large energy range, we use the effective-mass model described in Sec. III B. The advantage of the EMA method is that we can easily calculate a large number of eigenstates (not only near-gap states). This permits obtaining a good statistical description of the density of states and other global properties. We have thus modeled a 2000 ML Sasaki-type  $d$ -SL, obtaining all the states up to 1 eV away from the band edges. We calculated heavy-hole states for the hole and  $X$  valley states for the electron. The results are shown in Fig. 13. Each state is represented by a single horizontal line. The vertical position of the line indicate its energy and horizontal position denotes its point of localization. The length of each

line is  $2L_{\text{eff}}$  using the one-dimensional version of Eq. (16). Figure 13 shows that all states are localized, as expected from one-dimensional Anderson localization theory.<sup>29,30</sup> There is no transition from localized states to delocalized states. Around the band edge, the localization of the states is more properly described by the Lifshits theory.<sup>30</sup> Figure 13 gives the distribution of the  $d$ -SL states, in both energy and coordinate space.

One way to display the information in Fig. 13 more quantitatively is to calculate the density of states (DOS) and localization length  $L_{\text{eff}}$  as functions of energy  $E$ . We have calculated 100  $d$ -SL systems (each with 2000 ML as in Fig. 13) and averaged the results. The DOS as a function of energy is shown in Fig. 14(b). (Notice that the DOS calculated here are the DOS considering the  $\bar{\Gamma}$  point only, thus, truly one-dimensional DOS. If the lateral dimensions were considered, the shapes of the DOS would change.) For electron states, we calculated both the  $X$  valley states and  $\Gamma$  valley states. Notice that summing up these two density of states only makes sense for low-energy regions where two separate valleys are well defined. For high-energy regions, the states from  $X$  and  $\Gamma$  valleys may not be distinguishable, and thus are not well defined. They may correspond to a single state in

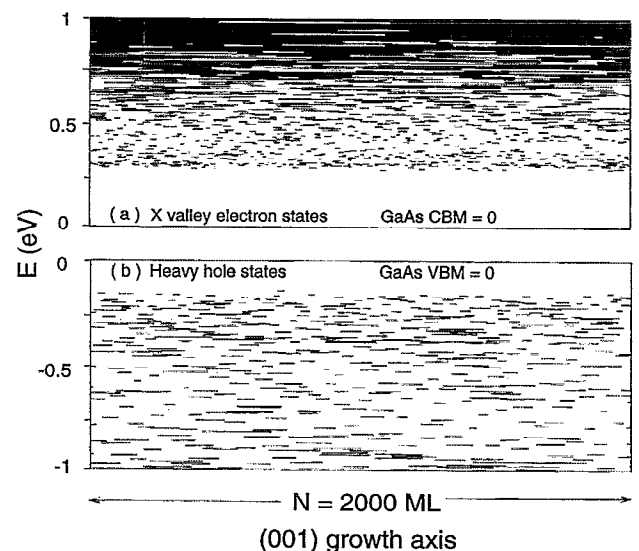


FIG. 13. Effective-mass calculated localized states of a 2000 ML  $d$ -SL. Each line represents one eigenstate. The line length equals  $2L_{\text{eff}}$ .

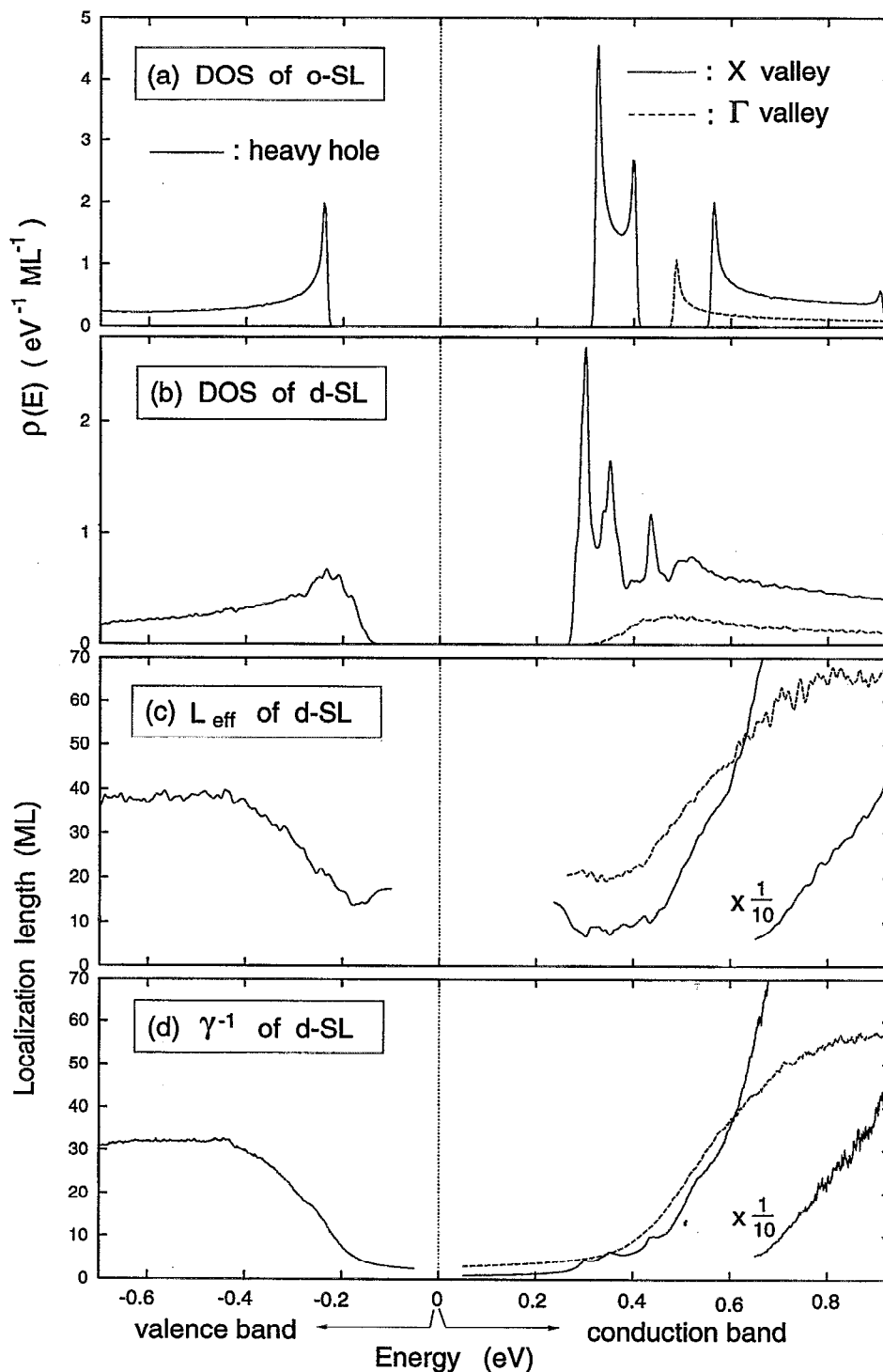


FIG. 14. Effective-mass calculated density of states of (a) the (001)-ordered  $(\text{GaAs})_2/(\text{AlAs})_2$  and (b) Sasaki-type disordered superlattices, and the localization lengths (c)  $L_{\text{eff}}$ , (d)  $\gamma^{-1}$  of the disordered superlattice. The conduction-band energy is measured from the bulk GaAs CBM and the valence-band energy is measured from the bulk GaAs VBM.

a multiband calculation. A very interesting fact is the peaks in the DOS of X valley electronic states. To understand these peaks, we have calculated the DOS for the  $(\text{GaAs})_2/(\text{AlAs})_2$  ordered superlattice. The results are shown in Fig. 14(a). It is evident that the peaks of X valley states of the  $d$ -SL in Fig. 14(b) are the remnants of the peaks seen in Fig. 14(a) for the  $o$ -SL with some shifts. On the other hand, for  $\Gamma$  valley states

and heavy-hole states, there is only one peak in the ordered superlattice, thus their DOS of  $d$ -SL have simple structures.

The effective localization length  $L_{\text{eff}}$  [Eq. (16)] is shown in Fig. 14(c). Notice that  $L_{\text{eff}}$  increases a bit near the band edge. As described by the Lifshits theory, this phenomenon is due to consecutive wide potential wells. At energy far away from the band edge,  $L_{\text{eff}}$  of the X valley electron states and

heavy-hole states bend down. Part of the reason is that we used the boundary condition of Eq. (9). As a result, for very large  $E$ , when the effect of the potential is no longer important, the mass confinement still plays an important role. This might not correspond to the real situation, because the effective mass model could fail in those energy regions. Another characteristic length of the states is the asymptotic decay length  $\gamma^{-1}$  as described in Sec. IV C. It turns out that this  $\gamma$  is just the exponential growth rate of  $A_{N+1}(E)$  [defined in Eq. (14), which does not equal  $A_1$  for arbitrary  $E$ ] as a function of  $N$ . If  $E$  is an exact eigenvalue  $\epsilon_i$  of an localized state, then  $A_{N+1} = A_1$ , thus, the magnitude of  $A_{N+1}$  is  $O(1)$ . However, the measure of these  $E \in \{\epsilon_i\}$  is zero, so in most cases  $A_{N+1} \propto e^{\gamma N}$ . Using this fact, we can calculate  $\gamma(E)$  from  $A_{N+1}(E)$  directly and the result is accurate and reliable. The  $\gamma^{-1}(E)$  are shown in Fig. 14(d). Note that, in the DOS tail region,  $L_{\text{eff}}$  is larger than  $2\gamma^{-1}$ , indicating Lifshits localization. For large energy,  $L_{\text{eff}}$  and  $\gamma^{-1}$  are close to each other. This can be understood by the fact that  $L_{\text{eff}} \sim \frac{4}{3}\gamma^{-1}$  for a localized wave function  $\cos(kz)e^{-\gamma|z|}$  with  $k$  much larger than  $\gamma$ . In Figs. 14(c) and 14(d) corresponding to the peaks of DOS for X valley states, its  $L_{\text{eff}}(E)$  and  $\gamma^{-1}(E)$  show dips and peaks, respectively. In the light of the peaks of the DOS, the dips of  $L_{\text{eff}}(E)$  and peaks of  $\gamma^{-1}(E)$  can be understood as follows. The existence of the eigenstates around a given energy  $E$  will slow down the exponential growth of  $A_{N+1}(E)$  [in the case of precise resonance,  $A_{N+1}$  will be  $O(1)$ ], thus  $\gamma^{-1}(E)$  increases. So a peak in the DOS will induce a peak in  $\gamma^{-1}(E)$ . On the other hand, because of orthogonalization, more eigenstates means less physical space for each state, hence the dip in  $L_{\text{eff}}(E)$ .

## 2. Disordered SLs with $\Delta n \approx n$ : Band-edge states and oscillator strength

We now focus on the band edges near the band-gap region. The band-edge states are involved in optical absorption and emission in the visible-light and near-infrared regions, and thus determine the optoelectronic properties of the  $d$ -SLs. First, we discuss the results of our pseudopotential calculations. In Fig. 11 we show the EPM-calculated dispersion of the band-edge states of the  $d$ -SL (solid lines) with  $p(1)=p(2)=p(3)=\frac{1}{3}$  along the symmetry lines  $\bar{\Sigma}$  and  $\bar{\Delta}$ . The thin horizontal lines denote the band edges of the underlying  $o$ -SL (see Sec. IV A). We find that the conduction bands of the  $d$ -SL dip below these lines. The difference (“binding energy”) increases in the order  $\bar{M} \rightarrow \bar{\Gamma} \rightarrow \bar{X}$ . The large binding energy at  $\bar{X}$  is a consequence of the level repulsion of the folded  $L_{1c}$  states, which is much stronger for odd values of the repeat period  $n$  than for even  $n$  [see Fig. 7(b)]. In the  $d$ -SL the odd-even selection rule is broken, leading to a stronger level repulsion in the  $d$ -SL than in the  $n=2$   $o$ -SL. Nevertheless, the large binding energy at  $\bar{\Gamma}$  pulls the conduction-band edge below the ones at  $\bar{X}$  and  $\bar{M}$  by 60 meV, making the  $d$ -SL a direct-gap material, even though the  $o$ -SL is indirect (with CBM at  $\bar{M}$ ).

In order to establish whether the direct transition does indeed lead to efficient recombination, we have to consider dipole matrix elements between the band-edge states involved in the optical excitation. Figures 15(c) and 15(d)

show a few band-edge wave functions of an  $N=1000$  ML  $d$ -SL, which are plotted using the planar average introduced in Fig. 9. For example, the states labeled CB3 and VB1 are localized at the same positions along the chain, and consequently their dipole matrix element can be large, whereas states with no spatial overlap will have a zero matrix element. From the dipole matrix element we obtain the oscillator strength  $f$  of an optical transition, which is defined as

$$f = \frac{1}{\hbar\omega} \frac{2|\langle c|\mathbf{p}|v\rangle|^2}{3m} \quad (17)$$

Here  $\hbar\omega$  is the transition energy,  $\langle c|\mathbf{p}|v\rangle$  the dipole matrix element between states  $|c\rangle$  and  $|v\rangle$ , and  $m$  the free electron mass. The factor of 3 in the denominator is introduced to average over the three polarizations  $x, y, z$ . In Table V we report calculated values of  $f$  for direct transitions in various systems. We see that

- (i) oscillator strengths of pseudodirect transitions in ordered SLs are 1–2 orders of magnitude smaller than those of the (higher energy) direct transitions,
- (ii) The transition between an extended state and a localized one (as occurs for the AIAs  $\delta$  layer, see Fig. 10) is of the similar strength as a pseudodirect transition,
- (iii) Transitions between two states that are localized in the same region along  $z$  are of comparable strength than the direct transitions in bulk materials.

Thus, the transition between the two localized states VB1 and CB3 in Figs. 15(c) and 15(d) is truly direct, rather than pseudodirect. The latter result explains the experimentally observed strong PL intensity.<sup>15</sup> The enhanced oscillator strength is reflected by short radiative lifetimes,  $\tau$ . We calculate  $\tau=1$  ns for the VB1→CB3 transition at energy 1.96 eV. These radiative lifetimes are 1000× faster compared to those measured in indirect-gap  $o$ -SLs ( $\tau \approx 5.5$   $\mu\text{s}$  at  $T=2$  K).<sup>54</sup> Furthermore, the calculated transition energy agrees very well with measured PL emission lines in  $d$ -SLs, which were found at  $\sim 1.96$  eV.<sup>65</sup>

We have seen that in ordered SLs the distinction between direct and pseudodirect transitions can be made by mapping SL states on “parent” states in the zinc-blende structure: Pseudodirect transitions at a SL wave vector  $\bar{\mathbf{K}}$  involve one folded state and one state genuine to  $\bar{\mathbf{K}}$ . An example is the  $\bar{\Gamma}(\Gamma_{15v}) \rightarrow \bar{\Gamma}(X_z)$  transition in (001) SLs (see Sec. IV A). While folding is not a very useful concept in a disordered SL (the height of the  $d$ -SL Brillouin zone is equal to  $2\pi/Nd$ ), the parentage of a  $d$ -SL state can still be defined in terms of its projection on zinc-blende states. We have performed such an analysis for a few conduction-band-edge states in (001)  $d$ -SLs. We found two types of states:

- (i) localized states whose projection on zincblende (ZB) states is peaked at the  $\Gamma$  point, and
- (ii) localized states whose projection is peaked at the  $X_z$  point of the ZB Brillouin zone.

In real space, the  $\Gamma$ -like states are localized in GaAs-rich regions [e.g., where a few  $(\text{GaAs})_n$  layers are separated by monolayer AIAs barriers], and the  $X_z$ -like states occur in AIAs-rich regions. This chemical selectivity reflects the

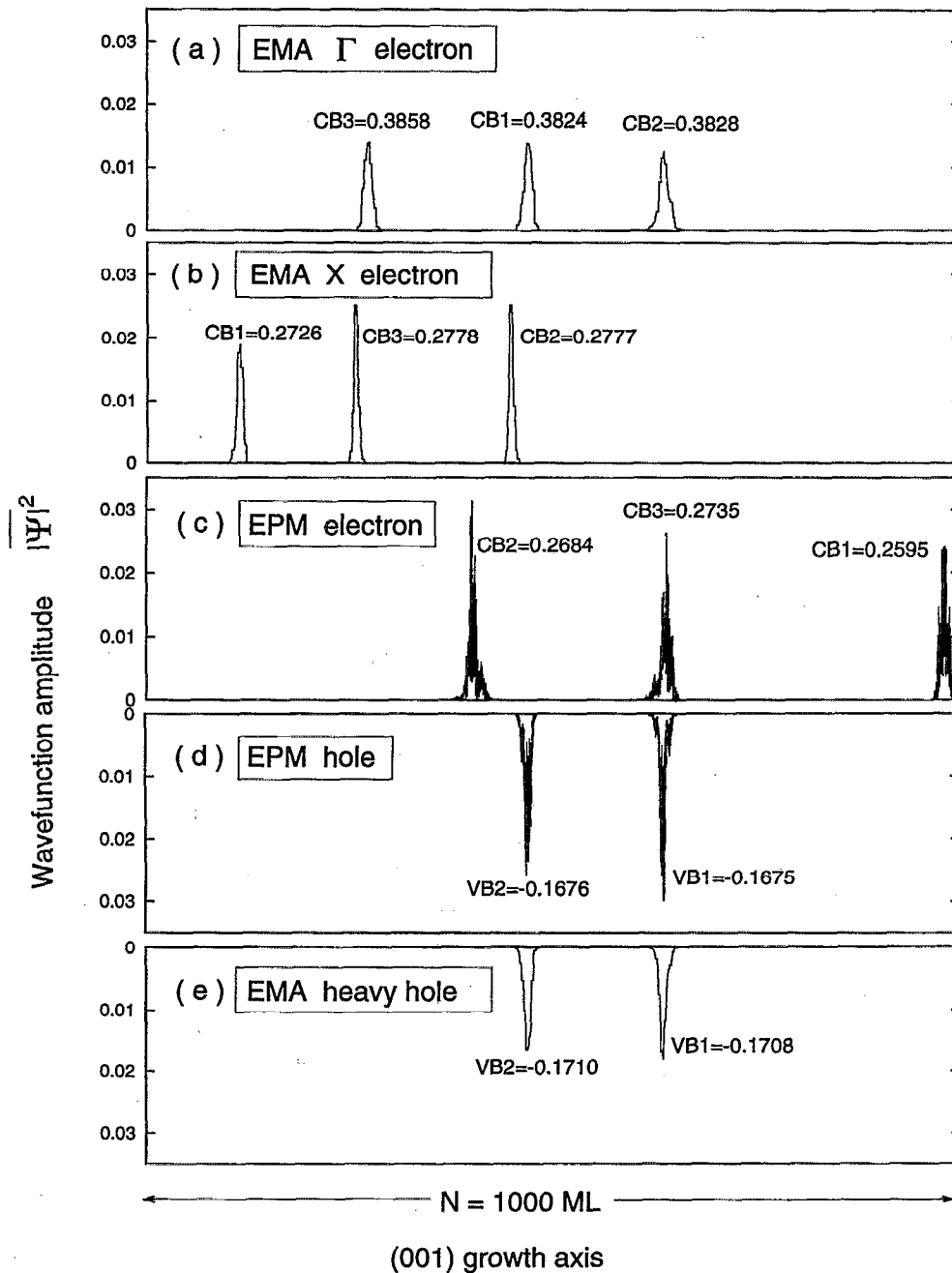


FIG. 15. The valence-band maximum states and conduction-band minimum states of a 1000 ML disordered superlattice, obtained by empirical pseudopotential model (EPM) and effective-mass approximation (EMA). The numbers are the eigenenergies of the states in eV. For the conduction-band states and valence-band states, they are measured from bulk GaAs CBM and VBM, respectively.

type-II band alignment of the ordered (001) SLs. Unlike in the  $2 \times 2$   $o$ -SL, however, the lowest states in the  $d$ -SL are the  $\Gamma$ -like states [e.g., all conduction states depicted in Fig. 15(c) are  $\Gamma$ -like]. Note that the  $1 \times 1$   $o$ -SL also has the  $\bar{\Gamma}(\Gamma_{1c})$  state below the  $\bar{\Gamma}(X_z)$  state [Fig. 7(b)]. This band order is not reproduced by the EMA, and we see below that also for the  $d$ -SL the EMA predicts the lowest conduction states to be  $X_z$ -like.

The localization lengths of the band-edge wave functions in the  $d$ -SL are comparable to those of the single  $\delta$ -layer-bound states (see Table III). This indicates that the

mechanism of localization in both cases is essentially the same, and that the localization is well described by chemical impurity binding to a single  $\delta$  layer. As one increases the concentration of  $\delta$  layers, an increasing number of bound states is introduced, which are degenerate at small concentration  $R$ . Unlike in the case of the periodic array of  $\delta$  layers, the bound states repel each other when  $R \rightarrow 1$ , and the band edges move further away from the unperturbed edges. Figure 12 shows via the diamond symbols the band-edge energies as a function of  $R$ , calculated for  $\sim 10$  different realizations of  $d$ -SLs at each  $R$ . The vertical bars centered on the configu-

TABLE V. Oscillator strengths of direct optical transitions in bulk materials, ordered (001) SLs,  $\delta$  layers in the  $2 \times 2$   $o$ -SL, and disordered SLs. The oscillator strength  $f$  is given in Eq. (17), where the initial state is always the valence-band maximum (in case of a degenerate VBM the squared dipole matrix elements are averaged over the degenerate manifold). For the disordered systems, the final states are identified in Figs. 9, 10, 15, and 16, respectively.

System	Final state	Energy (eV)	$f$
Bulk GaAs	$\Gamma_{1c}$	1.52	4.03
Bulk AlAs	$\Gamma_{1c}$	3.04	1.91
(AlAs) <sub>1</sub> /(GaAs) <sub>1</sub> $o$ -SL	$\bar{\Gamma}(\Gamma_{1c})$	2.02	2.21
	$\bar{\Gamma}(X_c)$	2.12	0.02
(AlAs) <sub>2</sub> /(GaAs) <sub>2</sub> $o$ -SL	$\bar{\Gamma}(X_c)$	2.09	0.08
	$\bar{\Gamma}(\Gamma_{1c})$	2.14	2.40
GaAs $\delta$ layer	CB1	2.04	1.67
AlAs $\delta$ layer	CB1	2.06	0.02
$d$ -SL	CB3	1.96	1.68
po-SL	CB1	1.87	2.76

rational averages give the size of the fluctuations of the eigenenergies. It is interesting to note that the band tail is larger for the conduction electrons than for the valence electrons. This asymmetry is contrary to expectations based on 1D one-band models, and reflects the strong band coupling and 3D character retained in our calculation. In a one-band model, localization effects decrease with increasing energy, because the kinetic energy becomes increasingly dominant over the (randomized) potential energy.

Also shown in Fig. 12 are the band-edge energies of the partially ordered SL (po-SL), which was studied experimentally by Arent *et al.*<sup>45</sup> The corresponding wave functions are depicted in Fig. 16. While the trends are similar to those observed in the  $d$ -SLs two distinct features are noteworthy:

(i) Occupied and unoccupied levels with corresponding

labels are localized at the same positions along  $z$ , i.e., CB1 and VB1+2, CB2 and VB3+4, etc., [see Fig. 16];

(ii) the band-gap reduction is slightly larger for the po-SL than for the  $d$ -SL at equal  $R$  (see Fig. 12).

Indeed, PL emission lines have been measured at energies as low as 1.87 eV,<sup>66</sup> in agreement with our calculated band gap of 1.87 eV. The CB1 and VB1+2 states are localized in a region where five (GaAs)<sub>3</sub> wells are separated by four (AlAs)<sub>1</sub> barriers. Similarly, the CB2 and VB3+4 states are localized in region with four 3 ML GaAs wells separated by three 1 ML AlAs barriers. Note that in the po-SL the probability of such a “one-dimensional clustering” is larger than in the  $d$ -SL. For example, the probability to find the molecule  $G_3A_1G_3A_1$  is equal to  $p(3)p(3) = (\frac{1}{3})^2$  for the po-SL, and equal to  $p(3)p(1)p(3)p(1) = (\frac{1}{3})^4$  for the  $d$ -SL, etc. [see Eq. (1)]. Furthermore, we saw that the particular molecule distribution function of the po-SL leads to LRO (see Fig. 4), which causes an enhancement of the structure factor  $|S(k_{||})|^2$  at certain wave vectors (Fig. 5). The structure factor enters the matrix elements pertinent to first-order perturbation theory, which could also explain why LRO present in the po-SL changes binding energies of localized states with respect to the  $d$ -SL.

Next, we calculate the Sasaki-type  $d$ -SL using the effective-mass model. The EMA results are also shown in Fig. 15, where they are compared with the EPM wave functions. We find very good agreement between EMA and EPM band edge states for the holes: The highest hole states are localized at the same spatial position with almost the same wave-function shape; the eigenenergies differ by only 3 meV. The wave functions are localized at positions where consecutive wide GaAs wells are separated by thin AlAs barriers.

For electron states, the situation is more complicated. For EMA states, again, the location of the localized states is simply determined by the geometry of the potential. For example, the EMA  $\Gamma$  valley states in Fig. 15(a) are localized where a few consecutive wide ( $n=3$ ) GaAs wells are separated by thin ( $n=1$ ) AlAs barriers. Thus, these EMA  $\Gamma$  valley states have the same locations as the EMA hole states, as evident from Figs. 15(a) and 15(e). The EMA  $X_c$  electron states [Fig. 15(b)], on the other hand, are localized where a few consecutive wide ( $n=3$ ) AlAs wells are separated by thin ( $n=1$ ) GaAs barriers. From the EMA calculations, we see that the  $X$  valley electron states have lower energies than the  $\Gamma$  valley derived states. The projection analysis described above showed that the EPM conduction-band-edge states are more  $\Gamma$ -like than  $X$ -like states. This is at variance with the EMA results: The  $d$ -SL has a pseudodirect band gap in the EMA description, and a truly direct gap in the EPM description.<sup>67</sup> However, for the wave functions we do get an agreement between EPM CB3 state in Fig. 15(c) and EMA  $\Gamma$  derived CB2 state in Fig. 15(a). Thus, the EMA can still be useful to describe some properties of the electron state in the  $d$ -SL. The fact that we do not get agreement for all other CBM states indicates that the EPM results are complicated by possible  $\Gamma$ - $X$  coupling.

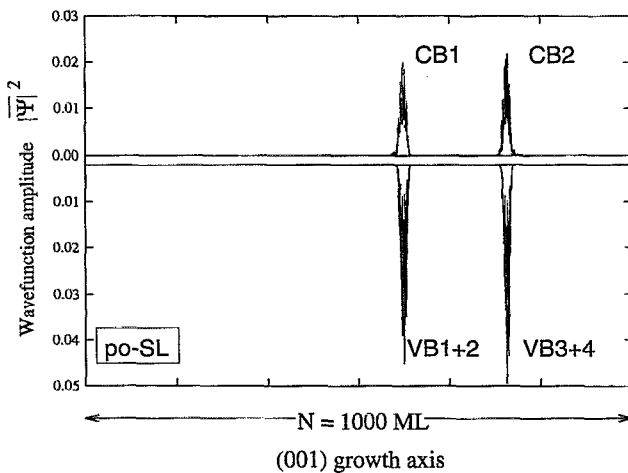


FIG. 16. Pseudopotential calculated planar average of the wave functions squared in a 1000 ML partially ordered SL (po-SL). Unoccupied states are labeled CB1, CB2,...; occupied states are labeled VB1, VB2,..., and are plotted in the negative direction with a small offset for clarity.

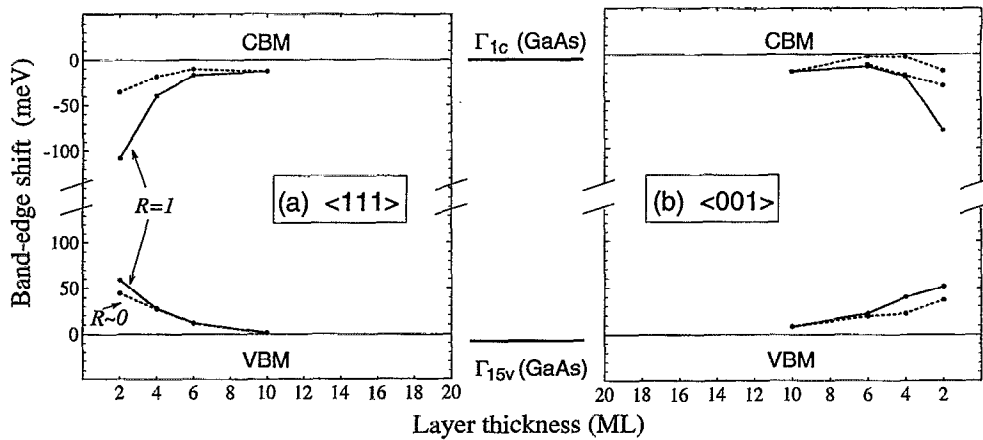


FIG. 17. Pseudopotential calculated gap levels in the presence of 1 ML thickness fluctuations in  $(\text{AlAs})_n/(\text{GaAs})_n$  superlattices along (a)  $\langle 111 \rangle$  and (b)  $\langle 001 \rangle$ , as a function of period  $n$ . Energies are measured with respect to the band extrema of the ideal  $n \times n$  SL (see Fig. 7).  $R=1$  and  $R \rightarrow 0$  denote, respectively, the concentrated and dilute limit of chain mutations [Eq. (3)].

### 3. Disordered SLs with $\Delta n \ll n$

We now generalize to arbitrary ideal repeat period  $n$ , while keeping the thickness fluctuations fixed at  $\Delta n = 1$  ML. The EPM-calculated band-edge shifts of  $(\text{AlAs})_n/(\text{GaAs})_n$  SLs with 1 ML thickness fluctuations about  $n$  are plotted in Fig. 17 relative to the band edges of the ideal SLs (the energy zero, see Fig. 7). We see that:

- (i) The band-gap reductions  $\Delta E_g = \Delta \varepsilon_h + \Delta \varepsilon_e$  decay with  $n$ , and have a definite dependence on superlattice direction; they are 166, 67, 29, and 14 meV for  $n=2, 4, 6$ , and 10 in the  $\langle 111 \rangle$  direction, and 133, 64, 36, and 27 meV in the  $\langle 001 \rangle$  direction, respectively;
- (ii)  $\Delta E_g(R \rightarrow 0)$  merges with  $\Delta E_g(R=1)$  at  $n \geq 6$ , at which point the gap reduction becomes independent (“band-gap pinning”) of the number of chain mutations.

In order to explain these findings, we discuss the intermediate case of the  $n=6$   $\langle 111 \rangle$  SL, where the VBM is already pinned (independent of  $R$ ), but where the CBM still shows dispersion with  $R$  (see Fig. 17). Figure 18(a) shows the CBM and VBM wave functions for the  $R=1$  SL. The CBM wave function is localized on  $\sim 4$  GaAs wells, with minimal amplitude in the AlAs barriers and maximal amplitude on the two neighboring mutated (7 ML) GaAs wells (“twin” fluctuation denoted by bold arrows). The CBM thus resembles a bound state in a coupled double quantum well. The hole wave function at the VBM is likewise localized on a number of mutated, 7 ML GaAs wells [Fig. 18(a)]; in contrast to the CBM, however, the reason for the multiwell pattern of the VBM wave function is that these states are in fact decoupled, quantum-well confined states, which are degenerate in energy within the accuracy of our calculation ( $\approx 0.1$  meV). A typical hole and electron wave function localized on an isolated  $(\text{GaAs})_7$  mutation in an otherwise ideal  $6 \times 6$   $\langle 111 \rangle$  SL are shown in Fig. 18(b). We see that the hole wave function of an isolated mutation ( $R \rightarrow 0$ ) resembles that of the concentrated ( $R=1$ ) mutations [Fig. 18(a)], and its binding energy  $\Delta \varepsilon_h(R \rightarrow 0) = 11$  meV equals the value at  $R=1$ . At the CBM, the larger penetration of the wave function into

neighboring GaAs wells can produce deeper gap states [see, for example, the twin fluctuation depicted in Fig. 18(a)], and consequently pinning occurs at a larger pinning period  $n_p \sim 10$  than for hole states.

Experimentally, the fluctuation-induced localized bound

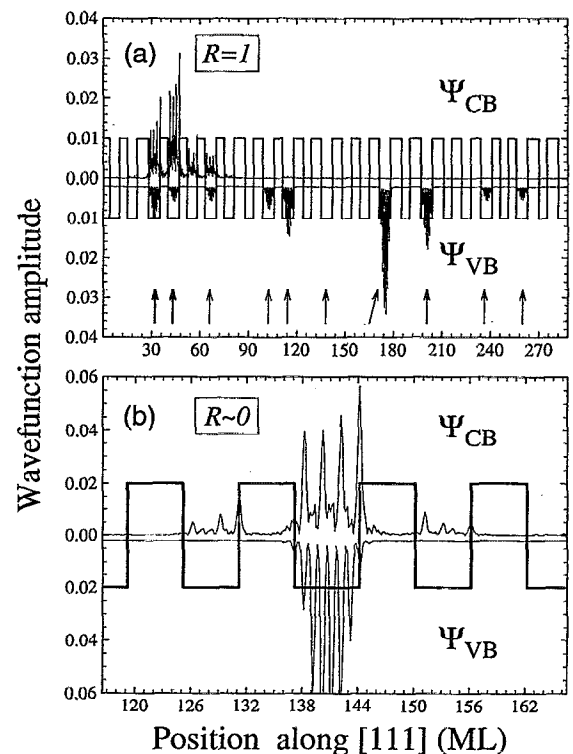


FIG. 18. Pseudopotential calculated planar averages of wave functions squared of the CBM and VBM in the  $(\text{AlAs})_6/(\text{GaAs})_6$  SL along  $\langle 111 \rangle$  with  $\pm 1$  layer-thickness fluctuations. Hole wave functions are plotted in the negative direction, with a small offset for clarity. (a) Concentrated limit ( $R=1$ ), (b) dilute limit ( $R \rightarrow 0$ ), i.e., a single  $(\text{GaAs})_7$  mutation embedded in a  $6 \times 6$  SL host. The rectangular lines show the growth sequence of the SL, with GaAs layers represented by wells, and AlAs layers represented by barriers, respectively. The vertical arrows in (a) indicate the 7-ML-thick, “mutated” wells.

states should be observable as photoluminescence centers whose energy is below the absorption edge of the underlying “ideal” SL structure. This photoluminescence will lack phonon lines, because the optical transitions are direct in the planar Brillouin zone (the transverse wave vector  $\mathbf{k}_\perp$  is still a good quantum number), and because the  $k_z$  selection rule is relaxed by vertical disorder. Indeed, while we have shown in Sec. IV A that ideal  $\langle 111 \rangle$  (AlAs) $_n$ /(GaAs) $_n$  SLs have a direct band gap with a type-I band arrangement, Cingolani and co-workers<sup>61</sup> noted a  $\sim 100$  meV red shift of the photoluminescence at 1.80 eV relative to the absorption in (AlAs) $_6$ /(GaAs) $_6$   $\langle 111 \rangle$  SLs, interpreting this as reflecting a type-II band arrangement. However, since they noted that their SL had a  $\pm 1$  ML period uncertainty, it is possible that the red-shifted photoluminescence originates from thickness-fluctuation bound states. Our calculated band gap of the  $n=6$  superlattice with  $\pm 1$  ML thickness fluctuations is 1.78 eV for  $R=1$ , and 1.80 eV for  $R \rightarrow 0$ , close to their observed photoluminescence peak position (1.80 eV).<sup>61</sup> Recall that chemical intermixing leads to a blue shift of the band gap (see Table II), whereas larger thickness fluctuation is needed to explain the observed 100 meV red shift.

Figure 17 shows that the bound states of isolated mutations ( $R \rightarrow 0$ ) merge with those of concentrated layer-thickness fluctuations ( $R \rightarrow 1$ ) at some pinning period  $n_p$ . At this point the band-gap reduction is pinned at the value

$$\Delta E_g(R) = \lim_{R \rightarrow 0} \Delta E_g(R) = \Delta \varepsilon_e + \Delta \varepsilon_h, \quad (18)$$

where  $\Delta \varepsilon_e$  ( $\Delta \varepsilon_h$ ) is the electron (hole) binding energy of an isolated ( $R \rightarrow 0$ ) layer mutation. Qualitatively, Eq. (18) can be understood in terms of the 1D effective-mass picture (Sec. III B). Each of the  $(n+1)$  ML mutations gives rise to a bound state below the band edge of the  $n \times n$  SL.<sup>20,14</sup> For very large  $n$ , when the quantum wells are completely decoupled (the tunneling probability and, hence miniband width, decrease exponentially with  $n$ ), the SL energy spectrum is simply that of degenerate single quantum wells of thicknesses  $n'$  with eigenenergies  $\varepsilon_v(n')$ . Hence, the extra binding energy of an  $(n + \Delta n)$  ML mutation approaches asymptotically

$$\Delta \varepsilon_c = \varepsilon_0(n) - \varepsilon_0(n + \Delta n) \approx \frac{2\Delta n}{n} \varepsilon_0(n), \quad (19)$$

where  $\varepsilon_0(n)$  is the ground-state energy of a carrier with mass  $m^*$  in an  $n$ -ML-wide quantum well, which scales like  $1/m^*n^2$  for large  $n$ . For example, using a fixed  $\Delta n/n = 10\%$ , rather than a fixed  $\Delta n$ , we obtain from the first equality of Eq. (19)  $\Delta \varepsilon_e = 10.0, 2.4,$  and  $0.7$  meV for  $n = 20, 50,$  and  $100$  in the  $\langle 111 \rangle$  SL [the last equality of Eq. (19) gives 14.3, 3.0, and 0.8 meV, respectively]. The band-gap reduction for a given  $\Delta n/n$  is obtained by inserting  $\Delta \varepsilon_h$  and  $\Delta \varepsilon_e$  from Eq. (19) in Eq. (18).

## V. CONCLUSIONS

Our main conclusions can be summarized as follows.

(a) (001)-ordered superlattices:

- (i) The  $n=1$  SL has an indirect band gap at  $\bar{K}$ ; Insufficient interfacial abruptness in the experimentally studied samples<sup>54</sup> leads instead to an X-derived CBM.
- (ii) For  $n < 4$ , the  $\bar{M}(X_{x,y}$  folded) states and the  $\bar{\Gamma}(X_z$  folded) states are nearly degenerate;
- (iii) The crossover from AlAs-like  $\bar{\Gamma}_{1c}(X_z)$  (type II) to GaAs-like  $\bar{\Gamma}_{1c}(\Gamma_{1c})$  (type I) happens around  $n=8$ .

(b) (111)-ordered superlattices:

- (i)  $\bar{\Gamma}_{1c}(\Gamma_{1c})$  is the CBM (type I) for all  $n$ ;
- (ii) There is a strong even-odd oscillation of the CBM energy due to mixing.
- (iii) Despite the prediction of direct gap of all (111)-ordered SLs, Cingolani and co-workers<sup>61</sup> found for  $n=6$  a type-II SL with a  $\sim 100$  meV red shift between absorption and PL; we find that lateral interfacial intermixing can not explain this discrepancy, but monolayer thickness fluctuations in the measured sample do resolve the disagreement.

(c) Single  $\delta$  layer doping in  $o$ -SL:

- (i) A (GaAs) $_3$   $\delta$  layer in (GaAs) $_2$ /(AlAs) $_2$  (001) SL produces an electron and a hole bound state with binding energies  $\Delta \varepsilon_e = 18$  meV and  $\Delta \varepsilon_h = 37$  meV, respectively;
- (ii) An (AlAs) $_3$   $\delta$  layer in (GaAs) $_2$ /(AlAs) $_2$  (001) SL produces only an electron bound state with  $\Delta \varepsilon_e = 33$  meV at  $\bar{\Gamma}$ .

(d) An ordered array of  $\delta$  layers:

The bound states in neighboring  $\delta$  layers start to have large interaction when their distance is less than 20 ML.

(e) A disordered SL with  $\Delta n \approx n$  (i.e.,  $n = 1, 2, 3$ ):

- (i) There is a 130 meV red shift in the band gap compared with the  $o$ -SL;
- (ii) The conduction-band minimum is at  $\bar{\Gamma}$ , not at  $\bar{X}$  as for the  $n=2$   $o$ -SL
- (iii) The conduction-band-edge states are more  $\Gamma$ -like than X-like, thus the oscillator strength is as large as the bulk GaAs value for a physically close electron-hole pair;
- (iv) The band-edge state localization length of the  $d$ -SL is about the same (20 ML) as the  $\delta$  layer bound state;
- (v) The localization lengths increase as the energy moves away from the band edge—all states are localized, so there is no mobility edge;
- (vi) The DOS of the  $d$ -SL has a peak near the edge of  $o$ -SL DOS and has a tail into the band-gap region; if the original DOS of the  $o$ -SL has several peaks, the DOS of the  $d$ -SL retains those peaks with some position shifts.

(f) A disordered SL with  $\Delta n \ll n$ :

For  $\Delta n = 1$  and  $n > 6$ , the band-edge energies are nearly pinned at their  $\delta$  doping level, independent of the magnitude of the disorder.

## ACKNOWLEDGMENTS

The authors thank Dr. S. H. Wei for many helpful discussions and advice. This work was supported by the office of Energy Research, Materials Science Division, U.S. Department of Energy, under Grant No. DE-AC02-83CH10093.

- <sup>1</sup>A. Ourmazd, D. W. Taylor, J. Cunningham, and C. W. Tu, *Phys. Rev. Lett.* **62**, 933 (1989).
- <sup>2</sup>J. Grant, J. Menendez, L. N. Pfeiffer, K. W. West, E. Molinari, and S. Baroni, *Appl. Phys. Lett.* **59**, 2859 (1991).
- <sup>3</sup>B. Jusserand, F. Mollot, R. Planel, E. Molinari, and S. Baroni, *Surf. Sci.* **267**, 171 (1992).
- <sup>4</sup>R. M. Feenstra, D. A. Collins, D. Z.-Y. Ting, M. W. Wang, and T. C. McGill, *J. Vac. Sci. Technol. B* **12**, 2592 (1994).
- <sup>5</sup>D. Bimberg, J. Christen, T. Fukunaga, H. Nakashima, D. E. Mars, and J. N. Miller, *J. Vac. Sci. Technol. B* **5**, 1191 (1987).
- <sup>6</sup>K. Fujiwara, N. Tsukada, T. Nakayama, and T. Nishino, *Appl. Phys. Lett.* **51**, 1717 (1987).
- <sup>7</sup>R. F. Kopf, E. F. Schubert, T. D. Harris, and R. S. Becker, *Appl. Phys. Lett.* **58**, 631 (1991).
- <sup>8</sup>I. Sugiyama, A. Hobbs, O. Ueda, K. Shinohara, and H. Takigawa, *Appl. Phys. Lett.* **58**, 2755 (1991).
- <sup>9</sup>C. Parks, A. K. Ramdas, M. R. Melloch, and L. R. Ram-Mohan, *Phys. Rev. B* **48**, 5413 (1993).
- <sup>10</sup>J. R. Meyer, A. R. Reisinger, K. A. Harris, R. W. Yanka, and L. M. Mohnkern, *Appl. Phys. Lett.* **64**, 545 (1994).
- <sup>11</sup>J. D. Dow, S. Y. Ren, and K. Hess, *Phys. Rev. B* **25**, 6218 (1982).
- <sup>12</sup>S. Das Sarma, A. Kobayashi, and R. E. Prange, *Phys. Rev. Lett.* **56**, 1280 (1986).
- <sup>13</sup>R. Merlin, K. Bajema, R. Clarke, F.-Y. Juang, and P. K. Bhattacharya, *Phys. Rev. Lett.* **55**, 1768 (1985).
- <sup>14</sup>A. Chomette, B. Deveaud, A. Regreny, and G. Bastard, *Phys. Rev. Lett.* **57**, 1464 (1986).
- <sup>15</sup>A. Sasaki, M. Kasu, T. Yamamoto, and S. Noda, *Jpn. J. Appl. Phys.* **28**, L1249 (1989).
- <sup>16</sup>C. A. Warwick and R. F. Kopf, *Appl. Phys. Lett.* **60**, 386 (1992).
- <sup>17</sup>V. I. Belitsky, T. Ruf, J. Spitzer, and M. Cardona, *Phys. Rev. B* **49**, 8263 (1994).
- <sup>18</sup>C. A. Warwick, W. Y. Jan, A. Ourmazd, and T. D. Harris, *Appl. Phys. Lett.* **56**, 2666 (1990).
- <sup>19</sup>M. J. S. P. Brasil, A. A. Bernussi, M. A. Cotta, M. V. Marquezini, J. A. Brum, R. A. Hamm, S. N. G. Chu, L. R. Harriott, and H. Temkin, *Appl. Phys. Lett.* **65**, 857 (1994).
- <sup>20</sup>R. K. Littleton and R. E. Camley, *J. Appl. Phys.* **59**, 2817 (1986).
- <sup>21</sup>H. X. Jiang and J. Y. Lin, *Superlattices and Microstructures* **3**, 689 (1987).
- <sup>22</sup>R. A. Davies, M. J. Kelly, and T. M. Kerr, *Appl. Phys. Lett.* **53**, 2641 (1988).
- <sup>23</sup>K. F. Brennan, *Appl. Phys. Lett.* **57**, 1114 (1990).
- <sup>24</sup>G. Ihm, M. L. Falk, S. K. Noh, and S. J. Lee, *Phys. Rev. B* **46**, 9564 (1992).
- <sup>25</sup>W. P. Su and H. D. Shih, *J. Appl. Phys.* **72**, 2080 (1992).
- <sup>26</sup>J. Strozier, Y. A. Zhang, C. Horton, A. Ignatiev, and H. D. Shih, *J. Vac. Sci. Technol. A* **11**, 923 (1993).
- <sup>27</sup>D. F. Nelson, R. C. Miller, C. W. Tu, and S. K. Sputz, *Phys. Rev. B* **36**, 8063 (1987).
- <sup>28</sup>M. Proctor, G. Oelgart, H. Rhan, and F.-K. Reinhart, *Appl. Phys. Lett.* **64**, 3154 (1994).
- <sup>29</sup>P. W. Anderson, *Phys. Rev.* **109**, 1492 (1958).
- <sup>30</sup>I. M. Lifshits, *Sov. Phys. JETP* **17**, 1159 (1963).
- <sup>31</sup>P. A. Lee and T. V. Ramakrishnan, *Rev. Mod. Phys.* **57**, 287 (1985).
- <sup>32</sup>P. Phillips, *Ann. Rev. Phys. Chem.* **44**, 115 (1993).
- <sup>33</sup>I. M. Lifshits, S. A. Gredeskul, and L. A. Pastur, *Introduction to the Theory of Disordered Systems* (Wiley, New York, 1987).
- <sup>34</sup>R. E. Borland, *Proc. R. Soc. London Ser. A* **274**, 529 (1963).
- <sup>35</sup>F. Laruelle and B. Etienne, *Phys. Rev. B* **37**, 4816 (1988).
- <sup>36</sup>K. Hirose, D. Y. K. Ko, and H. Kamimura, *J. Phys. Condens. Matter* **4**, 5947 (1992).
- <sup>37</sup>D. B. Laks, S.-H. Wei, and A. Zunger, *Phys. Rev. Lett.* **69**, 3766 (1992).
- <sup>38</sup>E. G. Wang, J. H. Xu, W. P. Su, and C. S. Ting, *Appl. Phys. Lett.* **63**, 1411 (1993).
- <sup>39</sup>E. G. Wang, J. H. Xu, W. P. Su, and C. S. Ting, *Appl. Phys. Lett.* **64**, 443 (1994).
- <sup>40</sup>E. G. Wang, W. P. Su, and C. S. Ting, *J. Appl. Phys.* **76**, 3004 (1994).
- <sup>41</sup>V. Kumar and G. Ananthakrishna, *Phys. Rev. Lett.* **59**, 1476 (1987).
- <sup>42</sup>X. Chen and S. Xiong, *Phys. Rev. B* **48**, 5273 (1993).
- <sup>43</sup>M. Kasu, T. Yamamoto, S. Noda, and A. Sasaki, *Appl. Phys. Lett.* **59**, 800 (1991).
- <sup>44</sup>A. Sasaki, *J. Cryst. Growth* **115**, 490 (1991).
- <sup>45</sup>D. J. Arent, R. G. Alonso, G. S. Horner, D. Levi, M. Bode, A. Mascarenhas, J. M. Olson, X. Yin, M. C. DeLong, A. J. SpringThorpe, A. Majeed, D. J. Mowbray, and M. S. Skolnick, *Phys. Rev. B* **49**, 11 173 (1994).
- <sup>46</sup>T. Yamamoto, M. Kasu, S. Noda, and A. Sasaki, *J. Appl. Phys.* **68**, 5318 (1990).
- <sup>47</sup>K. A. Mäder, L.-W. Wang, and A. Zunger, *Phys. Rev. Lett.* **74**, 2555 (1995).
- <sup>48</sup>K. A. Mäder and A. Zunger, *Phys. Rev. B* **50**, 17 393 (1994).
- <sup>49</sup>L.-W. Wang and A. Zunger, *J. Chem. Phys.* **100**, 2394 (1994).
- <sup>50</sup>B. Jonsson and S. T. Eng, *IEEE J. Quantum Electron.* **QE-26**, 2025 (1990).
- <sup>51</sup>If the  $\delta$  layers are arranged periodically in a host SL,  $R$  of Eq. (3) still bears the meaning of the "concentration" of  $\delta$  layers, and  $R \propto L^{-1}$ , where  $L$  is the (fixed) distance between the  $\delta$  layers.
- <sup>52</sup>S.-H. Wei and A. Zunger, *J. Appl. Phys.* **63**, 5794 (1988).
- <sup>53</sup>D. M. Bylander and L. Kleinman, *Phys. Rev. B* **34**, 5280 (1986).
- <sup>54</sup>W. Ge, W. D. Schmidt, M. D. Sturge, L. N. Pfeiffer, and K. W. West, *J. Lumin.* **59**, 163 (1994).
- <sup>55</sup>For  $n=5$  and  $n=6$  we find that the lowest conduction state at  $\bar{Z}$  is  $\approx 10$  meV lower than  $\bar{\Gamma}(X_2)$ , making these SLs indirect-gap materials (see Table III in Ref. 48); however, this energy difference is too small to allow a conclusive prediction on the pseudodirect/indirect nature of the band gap.
- <sup>56</sup>D. Wood and A. Zunger (unpublished).
- <sup>57</sup>D. B. Laks and A. Zunger, *Phys. Rev. B* **45**, 11 411 (1992).
- <sup>58</sup>S. B. Zhang, M. L. Cohen, S. G. Louie, D. Tomanek, and M. S. Hybertsen, *Phys. Rev. B* **41**, 10 058 (1990).
- <sup>59</sup>K. A. Mäder and A. Zunger, *Appl. Phys. Lett.* **64**, 2882 (1994).
- <sup>60</sup>Z. Ikonc, G. P. Srivastava, and J. C. Inkson, *Phys. Rev. B* **46**, 15 150 (1992).
- <sup>61</sup>R. Cingolani, L. Tapfer, and K. Ploog, *Appl. Phys. Lett.* **56**, 1233 (1990).
- <sup>62</sup>See, for example, G. Baym, *Lectures on Quantum Mechanics*, 9th ed. (Benjamin, Reading, MA, 1981), Chap. 4.
- <sup>63</sup>K. A. Mäder and A. Baldereschi, *Mater. Res. Soc. Symp. Proc.* **240**, 597 (1992).
- <sup>64</sup>C. Papantiantafillou and E. N. Economou, *Phys. Rev. B* **13**, 920 (1976).
- <sup>65</sup>M. Kasu, T. Yamamoto, S. Noda, and A. Sasaki, *Jpn. J. Appl. Phys.* **29**, L1588 (1990).
- <sup>66</sup>D. J. Arent (private communication). We used the same growth sequence for our computational unit cell as was used for the MBE growth of the po-SL.
- <sup>67</sup>This discrepancy can be traced back to the EMA error in the  $(\text{GaAs})_n(\text{AlAs})_n$ , o-SL of  $n \sim 1, 2$  in Fig. 7. Around  $n \sim 1, 2$ , the EMA  $\bar{\Gamma}_c(T)$  (001) states have much larger energies than their EPM counterparts. Apparently, this difference retains in the d-SL.